Analysis of the ability of titanium dioxide nanoparticles to produce singlet oxygen and hydrogen peroxide under ionising radiation

BSc thesis

Rebecca van den Elshout

July 2022

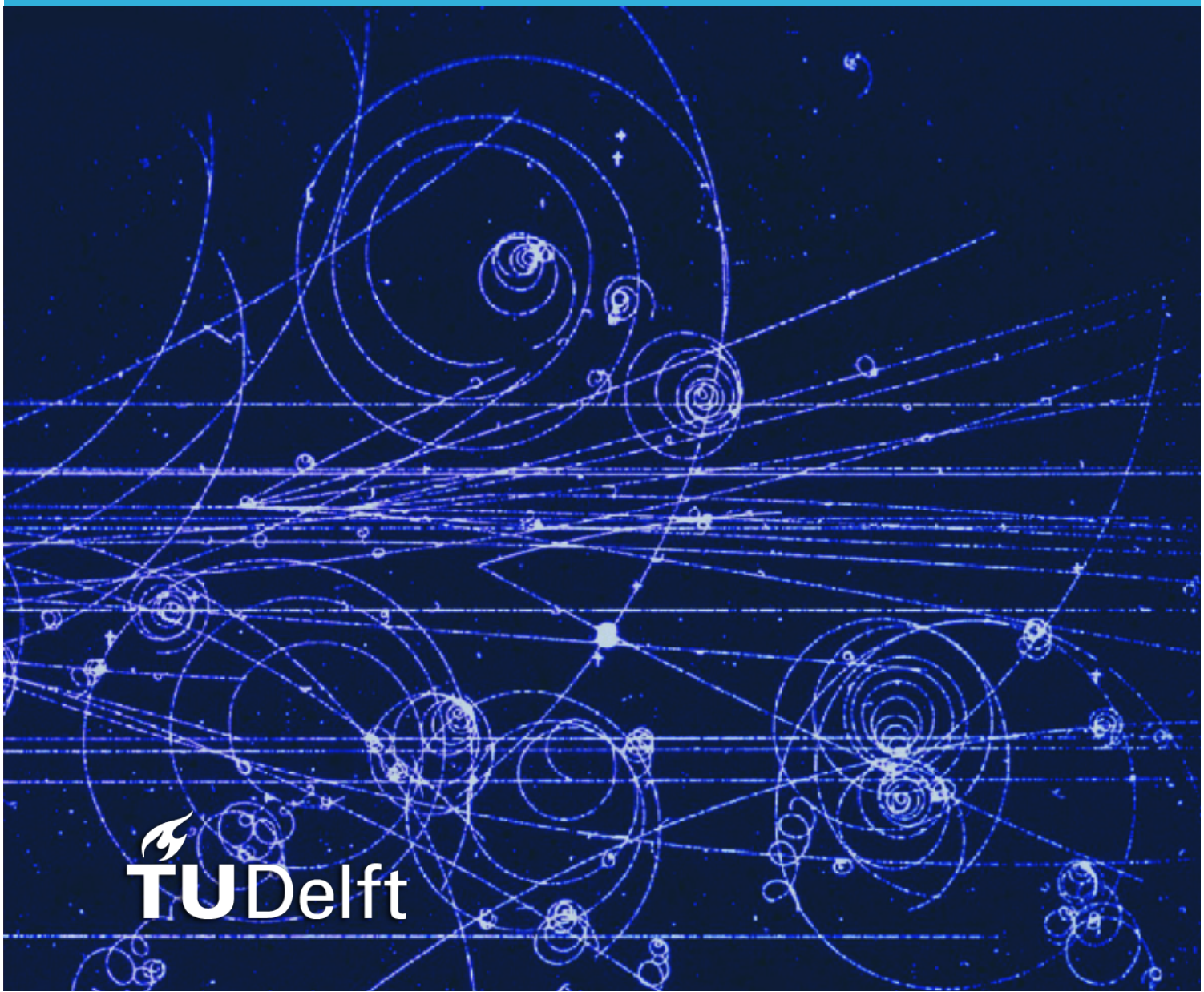

Analysis of the ability of titanium dioxide nanoparticles to produce singlet oxygen and hydrogen peroxide under ionising radiation

by

Rebecca van den Elshout

to obtain the degree of Bachelor of Science
at the Delft University of Technology,
to be defended publicly on Wednesday July 6, 2022 at 2:00 PM.

Student number:	5186889	
Project duration:	April 19, 2022 – July 6, 2022	
Thesis committee:	Dr. ir. A. G. Denkova,	TU Delft, supervisor
	Dr. ir. R. M. de Kruijff,	TU Delft
	Ir. B. Xu,	TU Delft, daily supervisor

An electronic version of this thesis is available at `http://repository.tudelft.nl/`.

TU Delft

Abstract

Radiotherapy is a vital component in the treatment of malignancies, with approximately 50 to 70% of cancer patients receiving it at some point. This therapy consists of irradiating the affected body part with an external beam of ionising radiation. A limitation of this technique is its damaging effect on healthy cells surrounding the tumour. Semiconducting nanoparticles could offer a solution to this, as these compounds can generate reactive oxygen species (ROS). ROS are a group of free radicals that are known to be able to damage DNA and potentially cause necrotic or apoptotic cell death. Using these metal nanoparticles could increase the radiation damage to malignant cells during radiotherapy, without raising the risk of cell death for the surrounding tissue.

Especially TiO_2 nanoparticles have been increasingly studied due to their ability to produce singlet oxygen, one of the most reactive ROS, while also having low toxicity and cost. However, many aspects of the ROS-formation remain unclear, including certain ROS production pathways. This report will therefore focus on the ability of TiO_2 to produce specific ROS in response to ionising radiation, which will primarily be compared to the ROS formation through the radiolysis of water. The focus lies on the detection of singlet oxygen and hydrogen peroxide (H_2O_2) after irradiation by either a Co-60 gamma or a low energy X-ray source over a range of 5 to 40 Gy. Their concentrations are detected by fluorescence spectroscopy for singlet oxygen, and by UV-VIS spectroscopy for hydrogen peroxide.

The results were promising for the use of TiO_2 in radiotherapy, with both MilliQ water and TiO_2 being able to produce singlet oxygen in increasing amounts over the entire researched irradiation range for both radiation sources; Moreover, TiO_2 could produce a significantly larger amount of this ROS than the MilliQ water samples did. The hydrogen peroxide detection experiments were first conducted with ZnO instead of TiO_2. During these, the trends observed for the H_2O_2 concentration were similar to the ones obtained during the singlet oxygen experiments. The main difference was that the ZnO samples produced approximately the same amount of H_2O_2 as the MilliQ water samples for X-ray irradiation, instead of higher values. Lastly, the hydrogen peroxide concentration in both TiO_2 and ZnO samples was measured after irradiation by Co-60. ZnO exhibited an upward trend in which the H_2O_2 molarity increased as the applied dose got higher. The detected H_2O_2 levels in the TiO_2 samples were, on the other hand, relatively stagnant. This observation is likely attributed to a relatively high extent of either the degradation, conversion, or adsorption of this ROS at the surface of TiO_2.

Contents

1 Introduction **3**

2 Theory **5**
2.1 Radiation . . . 5
2.1.1 Electromagnetic waves . . . 5
2.1.2 Gamma-rays and X-rays . . . 5
2.1.3 Photon interaction with matter . . . 6
2.1.4 Rate of energy transfer . . . 7
2.2 Cancer and radiotherapy . . . 8
2.2.1 Cancer - disease progression . . . 8
2.2.2 Formation of reactive oxygen species in water . . . 8
2.3 Metal nanoparticles as photosensitizers . . . 10
2.3.1 The use of nanoparticles in radiotherapy . . . 10
2.3.2 ROS formation at TiO2 surfaces . . . 10
2.3.3 Size and bioavailability of nanoparticles . . . 11
2.3.4 Chemical structures of TiO_2 and ZnO . . . 11
2.4 Experimental equipment . . . 13
2.4.1 Fluorescence spectrometry . . . 13
2.4.2 UV-VIS spectrometry . . . 13

3 Materials & Methods **14**
3.1 Radiation sources . . . 14
3.2 Materials . . . 14
3.2.1 Nanoparticles . . . 14
3.2.2 SOSG . . . 15
3.2.3 List of other chemicals . . . 15
3.3 Methods . . . 15
3.3.1 Detection of singlet oxygen . . . 15
3.3.2 Detection of hydrogen peroxide . . . 16

4 Results **17**
4.1 Detection of singlet oxygen . . . 17
4.1.1 Gamma irradiation . . . 17
4.1.2 X-ray irradiation . . . 18
4.1.3 Comparison between gamma and X-ray results . . . 18
4.2 Detection of hydrogen peroxide . . . 19
4.2.1 Gamma irradiation of MilliQ water and ZnO samples . . . 20
4.2.2 X-ray irradiation of MilliQ water and ZnO samples . . . 21
4.2.3 Comparison between gamma and X-ray results . . . 22
4.2.4 Gamma irradiation of TiO_2 samples compared to ZnO samples . . . 23

5 Discussion **24**
5.1 Formation of singlet oxygen by TiO_2 under gamma and X-ray irradiation 24
5.1.1 Comparison between the singlet oxygen production for TiO_2 and MilliQ 24
5.1.2 Comparison between singlet oxygen formation under gamma and X-ray irradiation . . 24
5.2 Formation of hydrogen peroxide by ZnO under gamma and X-ray irradiation 25
5.2.1 Comparison between hydrogen peroxide production for ZnO and MilliQ 25
5.2.2 Comparison between hydrogen peroxide formation for ZnO and MilliQ water under gamma and X-ray irradiation 26
5.3 Generation of hydrogen peroxide by TiO_2 27

6 Conclusion and Recommendations **28**
6.1 Conclusions 28
6.2 Recommendations 29

A Appendix **33**

1 Introduction

Cancer is one of the leading causes of morbidity worldwide. The global estimated incidence was 19.3 million in 2020, of which over 4 million new cases were reported in Europe during that same year alone [1, 2]. The disease is characterised by uncontrollable cell growth, which can start in almost any organ or tissue. The prescribed treatment often varies according to the cancer stage and the exact location within the body. Although the most common types are radiation therapy (also known as radiotherapy), chemotherapy and surgery [3], they are often used in combination with one another to increase the success rate. Furthermore, it has been estimated that 50%-70% of cancer patients receive radiotherapy at some point during their treatment [4]. Due to the importance of this kind of therapy, extensive research has been carried out on finding methods to improve its efficiency. This has resulted in a vast increase in the overall survival rates for a wide variety of malignant tumours [5].

In radiotherapy, an external beam of high-energy ionising radiation (such as gamma or X-rays) is applied to the patient's affected body part. A limitation of this technique is its effect on healthy cells surrounding the tumour. In fact, this is what limits the allowable dose of radiation to be received by the patient to the acceptable dose for the normal surrounding tissue [5]. Over the span of the last few years, the use of nanoparticles in radiotherapy has gained an increase in interest as they could offer a solution to this problem. Their key strength lies in their small size, as they have an diameter between 1 and 100 nm. Because of this, their surface area per unit volume is much larger than the ratio of their microparticle counterparts. This difference greatly increases their catalytic activity and reactivity. Semiconducting nanoparticles are of especially great interest for radiotherapy as they can generate reactive oxygen species (ROS)[6]. ROS are a group of free radicals that are highly reactive. Upon contact with organic matter, they can cause damage in various ways, including potential double-strand breakage of DNA and oxidation of other cellular components. These processes often lead to necrotic or apoptotic cell death, making metal nanoparticles an effective way to destroy cancer cells if present near malignancies[7].

TiO_2 has been especially well studied as a photosensitizing agent due to its ability to efficiently create ROS while also being readily available as well as having low toxicity and cost. Furthermore, it has been found that this photosensitizer molecule has the ability to produce singlet oxygen in the presence of O_2. Singlet oxygen ($^1O_2$), which has been identified as one of the most chemically reactive ROS, interferes with essential enzymatic processes within cells [8]. TiO_2 also has the potential to produce hydrogen peroxide (H_2O_2). Despite being less reactive than singlet oxygen, this ROS still has great potential in radiotherapy due to its ability to efficiently cause the death of cancer cells. Although it has already been proven that TiO_2 can increase radiotherapy results, many aspects of working with this nanoparticle remain unknown. For example, as water can also produce ROS in response to ionising radiation, it is difficult to distinguish the exact origin of the generated ROS during experiments as it is often necessary to bring TiO_2 into solution [9]. Additionally, TiO_2 has been observed to degrade the ROS it produces to its surface, making detecting these target compounds difficult. This problem is mainly encountered during experiments designed to detect generated H_2O_2 [10].

This thesis will focus on the effect of different doses of ionising radiation on ROS formation to gain a better insight into how TiO_2 could generate ROS during radiotherapy. The main focus will be on detecting singlet oxygen and hydrogen peroxide produced with an applied dose varying from 5 to 40 Gy of gamma or low-energy X-ray radiation. The relative amounts of singlet oxygen present after irradiation are measured with fluorescence spectroscopy, while the relative amounts and molarity of hydrogen peroxide are measured with UV-VIS spectroscopy. The obtained values thereof will be compared to the natural ability of water to produce ROS to get a clearer view of the degree to which TiO_2 nanoparticles could aid radiotherapy. In addition, the H_2O_2 production of TiO_2 will be compared to that of ZnO as this other metal nanoparticle kind degrades H_2O_2 to a lesser extent at its surface.

In the second chapter, the theory will be discussed, including the underlying principles behind radiotherapy and the use of nanoparticles herein. Chapter 3 gives a description of all radiation sources and chemical compounds used as well, as the methods for the experiments. Following this, chapter 4 will give an overview of the results, which will then be discussed in more detail in chapter 5.

2 Theory

2.1 Radiation

The relevant theory behind the thesis is discussed in the following sections. Subsection 2.1 covers the fundamentals behind radiation and how it can interact with matter. Subsequently, section 2.2 discusses how cancer is formed, how it progresses and how radiotherapy can be used as a treatment. Following this, section 2.3 describes how nanoparticles can aid radiotherapy. The main focus herein will be on TiO_2 and ZnO, and on their chemical properties. Lastly, section 2.4 will briefly discuss the theory behind fluorescence and UV-VIS spectrometers.

2.1.1 Electromagnetic waves

Electromagnetic radiation consists in its simplest form of energy that travels through a medium at the speed of light . It is emitted when a charged particle, for example an electron, is either accelerated or decelerated, and it comprises oscillating magnetic and electric fields that are transversely linked to one another [11]. One of the most important theories behind electromagnetic waves is Planck's quantum hypothesis. Herein, he introduced the concept that energy is quantized, meaning it can only possess discrete values. These values depend on the exact frequency of the wave and can be obtained by applying the following formula:

$$E = \frac{hc}{\lambda} \tag{2.1}$$

Here, h is Planck's constant, c the speed of light and λ the wavelength [12]. In the realm of quantum mechanics, these small packs of energy are called photons. When they are bundled together in a beam, the number density of these massless elementary particles directly correlates to the radiation intensity [11].

2.1.2 Gamma-rays and X-rays

Within the electromagnetic spectrum, there is an important distinction between two kinds of radiation: ionising and non-ionising. Out of these two, non-ionising radiation (e.g. radio waves and ultraviolet light) has the least amount of energy. It has the potential to let atoms vibrate, but not to produce changes within the molecule's electron cloud. Ionising radiation on the other hand (e.g. gamma- and X-rays) is able to convert atoms into ions due to the greater amount of energy it possesses. Moreover, this type of radiation has the potential to break intermolecular bonds due to its ionising effect. It is, however, not able to alter the nucleus' atomic structure with the relatively low energies used in this research. This means that, for example, gamma and X-ray radiation are able to alter the properties of the irradiated materials, but it is not able to make it radioactive. Although X-ray and gamma radiation both exhibit this same characteristic behaviour, their origin is slightly different [13].

The creation of these two types of radiation is directly linked to radioisotopes, which are atoms that possess unstable nuclei due to imbalances in neutrons and protons. To reach a state of stability, these nuclei often either emit α- or β-particles, which consist of both neutrons and protons for the former and solely of an electron or positron for the latter [13]. Another way of achieving stability is via a process called electron capture, in which an electron is absorbed by the nucleus. This electron is usually taken from the the two

innermost shells of the atom, the K- or L-shell. During electron capture, a proton is converted to a neutron while a neutrino is released. As the electron leaves behind a vacancy in the electron cloud, another electron from an outer orbital fills up its spot. This simultaneously causes the emission of X-ray photons as the lower orbitals are less energetic. The exact amount of energy with which these photons are emitted mainly depend on the so-called electron binding energy of the respective electron that moved to the lower shell [14].

As opposed to being produced in the electron cloud of an atom, gamma-rays originate in the nucleus. When a radioisotope decays to its daughter nucleus, it could have a surplus of energy as it might be raised to its excited state. To get from this to a stable condition, the nucleus can emit energy in the form of gamma-ray photons, thus causing it to fall back into a lower-energy state. In general, gamma photons have the highest energy compared to other forms of radiation in the electromagnetic spectrum and can thus penetrate further into irradiated materials [15].

2.1.3 Photon interaction with matter

Interaction between radiation and matter causes a flow of energy towards the irradiated material. Because photons in electromagnetic radiation do not have a charge, nor a mass, they exhibit unique interactions in which the range is essentially infinite as it is best simulated with an exponential law [13]. For both gamma radiation and X-rays, there are two main types of interaction between the photons and matter, namely the photoelectric effect and Compton scattering.

The photoelectric effect is the most dominant type of interaction for high-atomic-number materials at low energies. Herein, the energy of the photon is completely transferred to an electron if these two collide with one another. Due to this large energy transfer, the electron is ejected from its atomic orbital. As it usually loses most of its energy quickly, it will stay relatively close to the spot where it was originally removed from. The photoelectric effect especially occurs for atoms with high electron binding energies, where the energy of the photon only slightly exceeds these binding energies. The effect most often takes place in the K- and L-shells. Therefore, an electron from one of the more outer shells will move down to fill in this vacancy, thus emitting the characteristic X-ray radiation as mentioned in subsection 2.1.2.

For Compton scattering, the energy of the photon is only partially transferred to the electron. This effect mainly occurs for photons with a higher momentum. Just as with the photoelectric effect, an electron is ejected from its place in one of the electron orbitals, leaving behind a vacancy; However, because the photon retains some momentum, it is additionally scattered. It is important to note that the photon continues its way at a different angle θ than right before it hit the electron. Because of this, the Compton effect effectively creates a secondary radiation source within the irradiated material. The energy of this scattered photon depends on the angle of scattering and the energy the initial photon possessed. Unlike with the photoelectric effect, the probability of Compton scattering occurring is proportional to the electron density instead of to the atomic number [16].

The electron ejected from its orbital in the above two processes will have interactions with the surrounding tissue. Because of its charge, it can easily interact with nearby electrons even with no direct contact. If the electron travels through the medium with a large enough force, it has the potential to eject other electrons, causing ionisation. Another possible outcome is that the atom is raised to its excited state. Overall, the ionising effect of gamma- and X-rays is often not due to initial irradiation, but more so because of these secondary interactions by the ejected electrons with the surrounding medium. The third type of interaction with matter is pair production, which occurs for energies of 1.02 MeV and higher. Due to this large amount of required energy, the photon-nucleus interaction is able to convert energy into an electron and a position; However, this interaction is not relevant for medical applications because of this large energy threshold [16]. Figure 2.1 on the next page summarises the dominating effect at each atom number and photon energy.

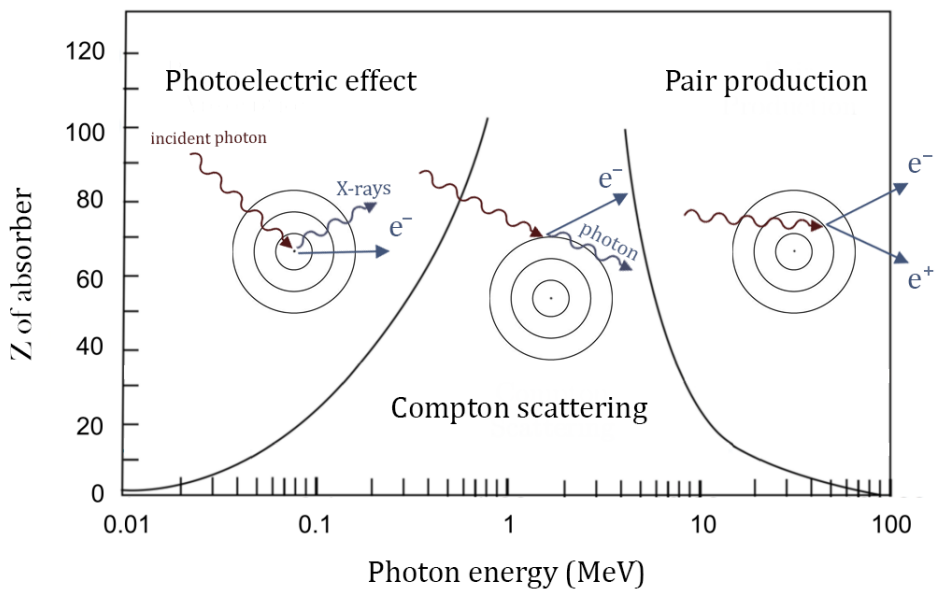

Figure 2.1: The three dominating photon interactions with matter are dependent on the atomic number of the irradiated material and the energy of the incident photons. The circles represent electron clouds, while the brown wavy arrows represent incident photons from either gamma- or X-ray irradiation. The blue arrows show the result of the interaction between the radiation and the matter.

2.1.4 Rate of energy transfer

An important term in radiation science is the Linear Energy Transfer (LET), which is a measure of the average amount of energy that is transferred per unit travelled length. The exact value highly depends on the kinetic energy. If the velocity of the electron decreases, the particle will lose its energy while the LET value increases. The effectiveness that certain radiation applications have is often expressed in terms of this LET, and it can be calculated by the following formula:

$$LET = \frac{Q^2}{E_k} \tag{2.2}$$

Here, Q is the charge of the particle and E_k the kinetic energy [17]. The exact relationship between the LET value and damage caused by the radiation differs per situation. As an example, for every biological effect, there is a certain optimal LET value that is able to produce an optimum energy concentration in the surrounding material. If radiation has a LET value that is too low, the amount of energy produced will be inadequate. On the other hand, too high LET values will deposit a surplus of energy needed to get the desired effect, meaning that energy and efficiency are wasted [16]. In general, gamma- and X-rays are classified as low-LET radiation, as compared to for example high-LET alpha particles [18].

Another important factor for radiotherapy is the Linear Attenuation Coefficient (μ). This coefficient is a measure of the fraction of photons that interacts with one cm of the irradiated matter. The primary factors that influence the attenuation are the thickness of the material, its density and the energy that the photons possess. As expected, photons with higher energies are more likely to penetrate deeper into the irradiated material compared to low-energy photons. Additionally, the probability of an interaction between a photon and matter increases exponentially with the distance travelled through the irradiated material. This exponential shape is best described by the Beer-Lambert law. For the Linear Attenuation Coefficient, the value primarily depends on the energy of the applied radiation and the atomic number of the irradiated material, as the latter influences the binding energy. The relationship is defined as follows:

$$I = I_0 e^{\mu x} \tag{2.3}$$

Here, I is the intensity of the transmitted rays, I_0 the intensity of the incident rays, x the thickness of the material and μ the linear attenuation coefficient. Hence the total attenuation can be found as follows [19]:

$$ln(\frac{I_0}{I}) = \int \mu(x)dx \tag{2.4}$$

It is important to note that the total attenuation rate depends on both the photoelectric effect as well as on Compton interactions. Therefore, the complete coefficient is built up according to the sum of the individual factors:

$$\mu_{(total)} = \mu_{(photoelectric)} + \mu_{(Compton)} \tag{2.5}$$

2.2 Cancer and radiotherapy

2.2.1 Cancer - disease progression

The general term cancer refers to a group of diseases that is characterised by cells that grow uncontrollably. The disease can start in almost every organ or tissue of the body, and is caused by damage to the DNA within a cell. This damage is often inflicted by either chemical compounds with carcinogenic properties or ionising radiation. Both of these can cause mutations by altering the nucleotide sequences of DNA. Generally, the cell is able to repair minor damages to its genetic material; However, successive mutations might result in the disruption of regular cellular physiology and could obstruct the function of vital genes. Especially mutations in proto-oncogenes, which mainly encode proteins for cell proliferation or the inhibition of apoptosis, can cause these genes to become oncogenes. This results in the characteristic uncontrollable growth of cancer cells, which could be magnified by additional mutations in tumour suppressor genes. This growing mass of cells could then develop into a malignant tumour, which can interfere with the function of an organ, potentially leading to organ failure. [20, 21]. In further stages, cancer can spread through the body in a process called metastasis, which could cause the growth of new tumours in other tissues or organs [22].

2.2.2 Formation of reactive oxygen species in water

The most important underlying mechanism for radiotherapy is the radiolysis of water, in which reactive oxygen species (ROS) are formed due to the interaction of the ionising radiation with water. A wide variety of compounds can be formed, which includes reducing species (e.g. H· and H_2), oxidising species (e.g. O_2·, O_2^-·, OH·, O_2) and a variety of stable molecules [23]. Examples of the ROS species that could be formed during radiolysis are shown in Figure 2.2.

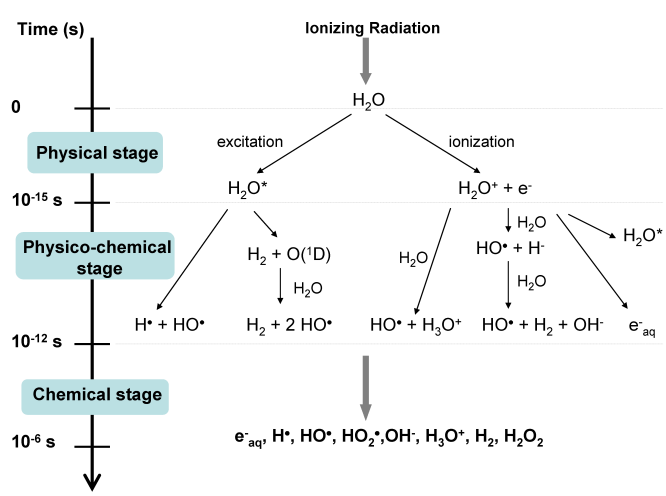

Figure 2.2: Schematic of the possible ROS species that could be formed during the radiolysis of water in response to ionising radiation [24].

As can be seen in Figure 2.2, radiolysis consists of three main stages. The first one, the physical stage, takes place approximately 1 fs after the ionising radiation gets into contact with the irradiated material. It is characterised by an energy deposition, which is then followed by relaxation processes. This causes either the transition from H_2O into ionised water (H_2O^+) or into sub-excitation electrons paired with excited water molecules. The second stage is the so-called physico-chemical stage which is characterised by a multitude of reactions that could take place. These include, but are not limited to, auto-ionisation of excited states and ion-molecule reactions. The chemical stage is the last phase and comprises the newly produced species being diffused into the solution and reacting with other particles, thus creating the final ROS. Which exact products are formed is highly dependent on several parameters, including the LET value and the pH of the solution. For example, high LET particles tend to cause radicals to recombine more easily, causing the formation of molecular species. Additionally, continuous irradiation by high-LET irradiation can lead to an increase in the formation of hydrogen peroxide (H_2O_2) compared to low-LET irradiation [24].

Radiotherapy and DNA damage

The use of ionising radiation in radiotherapy can induce DNA damage in a variety of ways. One of the most direct mechanisms is that high-energy radiation can cause double-strand breakage (DSB) in the DNA by damaging the phosphate backbone. The indirect method is characterised by the formation of ROS species through radiolysis. These chemical compounds can in turn cause damage by oxidising the nucleoside bases. As a result thereof, transversion of nucleotides could occur. Both this direct and indirect pathway are shown in Figure 2.3. It should be noted that there normally are repair mechanisms in place to ensure that oxidised bases are restored; However, if oxidisation takes place on both DNA strands simultaneously, carrying out this repair mechanism could lead to increased risks of DSB. Besides this kind of drastic damage to the DNA, ROS species can also cause other DNA lesions and additional degradation and breakage of mitochondrial DNA [25].

These changes to the DNA by ROS can eventually cause cell death. Cells that are dividing rapidly are namely more susceptible to the damage of ROS compounds, as compared to cells that divide relatively slowly [26]. The difference in sensitivity could theoretically ensure that the minimum radiation dose is strong enough to eliminate tumours, while not affecting the surrounding healthy cells. This is rarely achievable in practice as cancerous cells have the tendency to develop a resistance against radiation. The aforementioned factors consequently result in the need for elevated radiation doses, increasing the risk of damaging and killing normal tissue [6]. The exact dose that is administered to a patient depends highly on the tumour and its location, with most breast malignancies, for example, being irradiated with an overall dose of 45 - 60 Gy [27]. This dose is administrated during multiple sessions of usually 2 Gy each, in the span of approximately a month. The radiation that is used for this is generally in the range of 6 - 8 MeV.

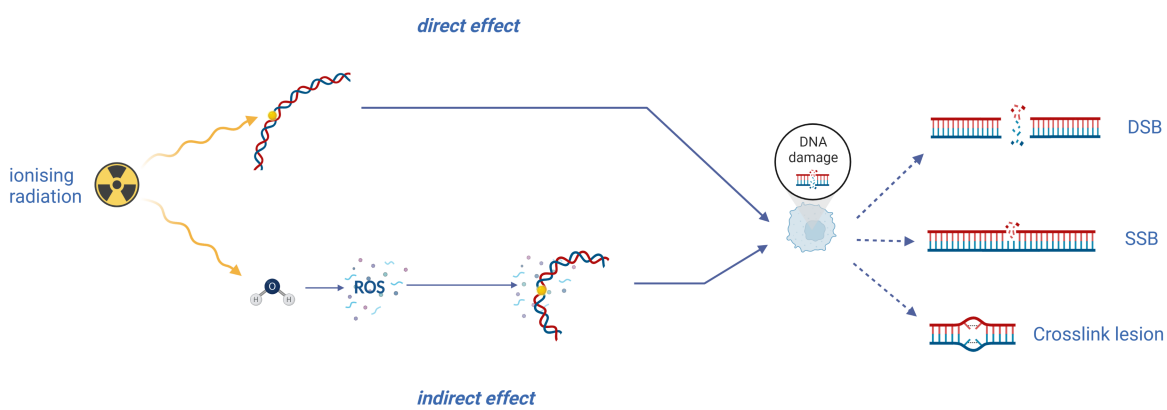

Figure 2.3: The two pathways along which ionising radiation can cause DNA damage. For the direct effect, the irradiation interacts immediately with the DNA. For the indirect effect, the radiation causes the conversion of water into Reactive Oxygen Species, which in turn can attack DNA. The damage to the DNA can consist of, but is not limited to, double-strand breakage (DSB), single-strand breakage (SSB) and cross-linking.

2.3 Metal nanoparticles as photosensitizers

2.3.1 The use of nanoparticles in radiotherapy

Approximately thirty years ago, the use of radiosensitizers was introduced into radiation therapy. These compounds or drugs are administered to patients to make tumours more sensitive to ionising radiation. The first materials that were thoroughly studied for these potential dose enhancers were high-Z materials that could be delivered to patients interstitially or via intravenous injection [28]. They generally exhibit a high photoelectric and scattering cross-section, which enables them to create secondary electron emissions upon interaction with ionising radiation [29]. Especially the use of gold nanoparticles (GNP) has been heavily investigated for this. When using regular particles, there often is only one high-Z atom per unit; However, by using nanoparticles, it becomes possible to use up to a few thousand high-Z compounds per nanoparticle unit. An additional major advantage is the great tunability of the shape and the size of nanoparticles [28]. It has been observed that when using low concentrations of GNPs, great local dose enhancement could be achieved while the overall dose for the irradiated organ or tissue stays approximately the same as without the use of these enhancers [29].

Lower-Z atoms generally have a less toxic effect on the human body than high-Z atoms, making them better-suited photosensitizer materials for the patient's safety. Especially the semiconductingTiO_2 has been increasingly studied due to its high compatibility with cells and the relatively large amount of ROS that is generated when this oxide is irradiated [30]; Furthermore, this photosensitizer has the ability to produce singlet oxygen in the presence of O_2. Singlet oxygen has been identified as one of the most chemical reactive ROS. This compound can interfere with essential enzymatic processes, thus efficiently leading to cell death [8]. It has already been established that the ROS formation for TiO_2 is rather effective when the compound is exposed to non-ionising radiation, such as UVA-rays and light in the visible spectrum. Despite these promising results, there are still many uncertainties about how exactly TiO_2 forms ROS under gamma irradiation or X-ray exposure. Over the years, many other semiconducting nanoparticles have been studied as well for their photosensitising effects. These include zinc oxide (ZnO), of which the exact ROS producing mechanism is not fully understood either [31].

2.3.2 ROS formation at TiO2 surfaces

As a photosensitizer, TiO_2 and ZnO are activated under light, which causes the formation and relaxation processes of electrons and holes on the surface of these molecules. One of the most suited methods for understanding this electron-hole mechanism, which causes the formation of ROS, is transient absorption spectroscopy due to its high temporal resolutions [32].

Both TiO_2 and ZnO are semiconductors. They have a valance band which contains electrons, and a conduction band which is free of these charged particles. The difference in energy between these bands is called the energy gap (Δ E) and indicates how much energy is required to excite an electron. This band gap energy is 3.37 eV for ZnO, and 3.20 eV for TiO_2. Both values are similar to the photon energy of electromagnetic radiation wavelengths of less than 400 nm. If the energy of the radiation is equal to the required excitation energy or exceeds it, an electron moves from the valence band to the conduction band. This leaves behind a vacancy in the valence band, a so-called positive hole. The bound state that results out of this is referred to as an exciton. It is unstable and exhibits characteristic redox properties. Both of the charged particles from the electron-hole pair are referred to as charge carriers. They usually move up to the surface of the atom where they can come into contact with adsorbed molecules. The interaction between the charge carriers and these molecules (for example H_2O) can cause the formation of ROS. The excited electrons are especially known for reducing oxygen (O_2) to the superoxide $O_2^{-}\cdot$; Moreover, the positive holes are prone to oxidising H_2O molecules to hydroxyl radicals (OH·) and hydrogen peroxide (H_2O_2). These pathways are shown in Figure 2.4. The figure also includes other conversions that are likely to take place at the surface of TiO_2 and ZnO particles. Another mechanism in which ROS can be formed is the inverse process of the one just described, namely the decay of an exciton; Herein, the recombination of an electron-hole pair occurs in a process called radiative recombination. During this, a photon is emitted in response to the excess energy.

This can cause the ground state of, for example, O_2 to be excited, which could in turn cause the formation of singlet oxygen $^1O_2$ [33].

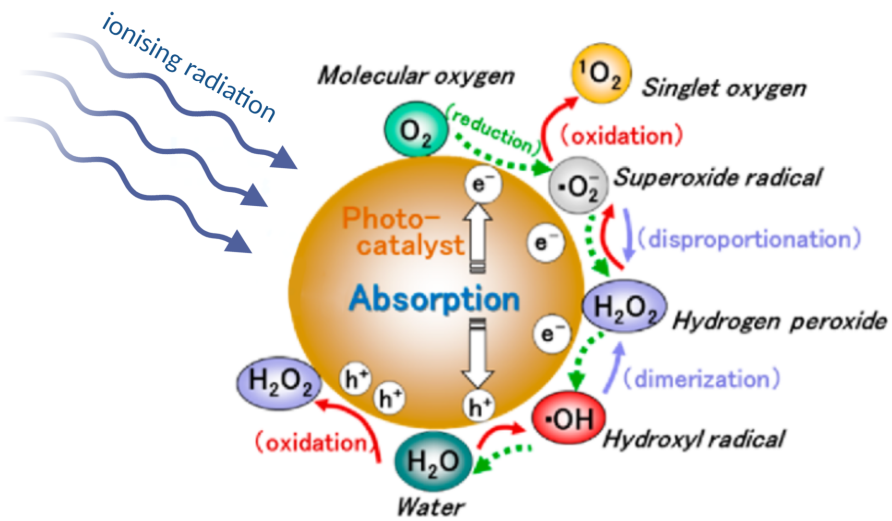

Figure 2.4: Possible mechanisms for Reactive Oxygen Species formation at the surfaces of TiO_2 and ZnO nanoparticle [34].

Both TiO_2 and ZnO are considered to be promising compounds to increase the effects of radiotherapy. Multiple studies have concluded that both semiconductors have the same therapeutic effect in photodynamic therapy (PDT). PDT is a less invasive procedure compared to radiotherapy, which involves the use of a photosensitising agent that is activated under a light source [35]; However, for radiotherapy, it is still unknown which of these two nanoparticle compounds yields better results. Although both are known to produce ROS, the exact species and their quantities produced under certain doses are still disputed.

2.3.3 Size and bioavailability of nanoparticles

The small size of nanoparticles increases the available surface area as compared to their microparticle counterparts. This causes the nanoparticles to be much more reactive, as more electron-hole pairs can diffuse to the surface and more molecules can be adsorbed from the surrounding solution. In general, smaller nanoparticles result in longer retention times in the blood. Particles with sizes of ≤ 10 nm are generally undesirable for medical applications as, although they penetrate deeply into tumours, they are toxic to healthy tissue. Compared to that, particles with a size of $10 <$ and ≤ 100 nm are still able to penetrate efficiently into tumours without being taken up by healthy cells in relatively large quantities [33]. Most reports on the development of cancer treatment with nanoparticles describe that the particles would be administered intravascularly. The injection site would dependent on the degree of metastasis as well as the kind of tumour. The nanoparticles could have to go through the blood circulation multiple times before being taken up by the malignancy, as the injection site can be relatively far away from the tumour [36].

2.3.4 Chemical structures of TiO_2 and ZnO

TiO_2 can be found in nature as one of three polymorphs: anatase, rutile, or brookite. All of these structures consist of a distorted octahedral shape in which every titanium atom is connected to six oxygen atoms. The exact chemical structures are shown in Figure 2.5 [37]. Out of these three, rutile has the narrowest band gap with an energy of around 3.0 eV. This is one of the main contributing factors to this TiO_2 conformation having the lowest photocatalytic activity. In general, anatase and rutile have been better studied

than brookite due to the complexity of the brookite synthesis procedure. There have been some studies on the photocatalytic activity of brookite, but with varying opinions on whether the use of this polymorph is justified regarding the synthesis process compared to the potential use for future applications. A recent study by Zerjav et al. gives a better insight into the photosensitising effects of all three chemical structures of TiO_2 and how they compare to one another [38].

Previously, it has been found that there is a synergistic effect for the photocatalytic activity between rutile and anatase. Mixed solutions of these two TiO_2 phases exhibited better photosensitising effects than either of the pure polymorphs. Although it is still unknown why exactly this effect occurs, it is likely attributed to the improved separation of UV-light generated charge carriers. Zerjav et al. conducted similar experiments and found that for this synergistic effect to happen, it is crucial that the anatase and rutile particles have approximately the same diameters and that other specifics (e.g. electronic properties) are also more or less identical. In the same study, it was also concluded that the low photocatalytic activity of rutile can be attributed to its deep e^- traps, which hinder electrons from being able to reach the surface of TiO_2. This also causes low charge carrier generation and a high rate of charge carrier recombination.

Of the three structures, anatase is often considered the best photosensitizer. This can be linked to its high specific surface area, and the long lifetime of the charge carriers due to anatase being an indirect band gap semiconductor, while rutile and brookite have a direct band gap. Zerjav et al. found that brookite can be comparable to anatase given a sufficiently large specific surface area. It would especially be a suitable alternative if the number of generated holes and the lifetime of the generated charge carriers are the limiting factors [38]. Besides the molecular interface of TiO_2, the size of the nanoparticles also seems to play an important role. Previous studies have concluded that both the photocatalytic activity as well as the amount of ROS produced from TiO_2 are directly proportional to the available surface defect sites. Smaller particles usually have a lower number of these sites, resulting in a lesser activity. In a study published by Jiang et al., an S-curved correlation was found between the ROS-producing activity and the nanoparticle size used; However, the authors warned that the exact values are highly susceptible to differences in the synthesis methods [39].

ZnO can normally be found as one of three different polymorphs: zinc-blende, wurtzite, and rock-salt. Out of these, wurtzite is most commonly encountered, as it is the most stable configuration at atmospheric pressure [40]. Although multiple studies have worked with ZnO to look into the ROS-producing capabilities of this semiconductor, little research has been carried out on comparing the photosensitising effects of the different ZnO configurations. It seems that most studies use wurtzite during their experiments, with little to no comments or data on the photosensitising effects of zinc-blende and rock-salt.

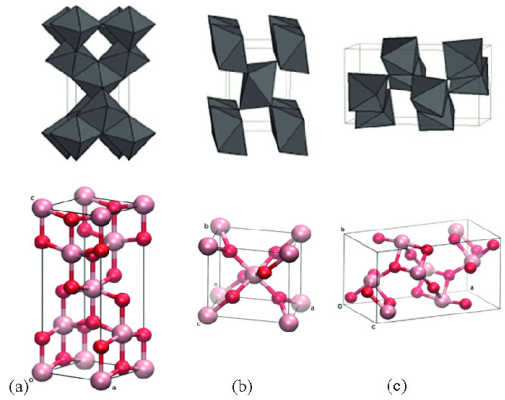

Figure 2.5: The crystal structures of the three TiO_2 polymorphs. Subfigure (a) displays anatase, (b) rutile, and (c) brookite [41].

2.4 Experimental equipment

Both fluorescence and UV-VIS spectrometry will be used in the experiments for this report to respectively detect singlet oxygen and hydrogen peroxide. The following two subsections will briefly discuss how these techniques work and how they are used to measure the ROS levels in samples.

2.4.1 Fluorescence spectrometry

The use of fluorescence spectrometers has become a reliable and relatively cheap method to measure the concentration of analytes in solutions. During the analysis, a beam of light, usually ultraviolet light, is shone through a liquid sample. This is preferably done at room temperature, as most molecules within the solution will then be at their ground electronic state. These molecules will absorb part of the light beam during the measurement, causing them to be elevated to one of their excited states. After having reached a higher vibrational level, they will eventually fall back to their ground state. During this process, the molecules emit the excess energy as fluorescence due to the energy levels of the ground state being lower than those of the excited states. The spectrometer detects these emitted photons and converts their energy levels to a unit called intensity. As fluorometers have both emission and excitation monochromators, they can display absorption spectra with the intensity on the y-axis and the corresponding wavelength on the x-axis [42].

The Singlet Oxygen Sensor Green (SOSG) probe will be used during the experiments to detect singlet oxygen with fluorescence spectroscopy. This indicator emits blue fluorescence in its pure state, and a green fluorescence when it is coupled to singlet oxygen. The excitation maxima for this is at approximately 504/525 nm [43]. Conclusions about the concentration of the singlet oxygen present in the samples can then be drawn by analysing the peak intensity around those wavelengths.

2.4.2 UV-VIS spectrometry

UV-VIS spectroscopy, short for ultraviolet-visible spectroscopy, is a powerful tool to identify and quantify compounds in solutions. The spectrometer requires two cuvettes with liquid samples, one which functions as a background measurement and one that has to be analysed. A beam of light will be shone through the two samples separately. The solutions will then absorb part of the light as the photons can cause transitions between the electronic energy levels of the molecules in the solution. The energies required for these transitions are characteristic of specific chemical species. To obtain the absorbance spectrum, the spectrometer records the absorption at specific wavelengths with the blank sample as comparison [44].

To detect the hydrogen peroxide in the samples, two stock solutions have to be added before spectrometric analysis can take place. The exact composition of these stock solutions is discussed in chapter 3 and is based on similar previous studies [45]; Therefore, it is known that H_2O_2 can be detected at 350.0 nm in the absorbance spectrum, where the absorbance in a.u. is plotted against the wavelength of the light shone through the solutions. It is possible to subsequently convert the absorbance measured at this wavelength to the H_2O_2 molarity by using a calibration curve that was created for the specific UV-VIS spectrometer and chemicals used.

3 Materials & Methods

This chapter gives a brief overview of the equipment and chemicals used for the experiments, with section 3.1 first describing the radiation sources, including the corresponding dose rates. Following this, section 3.2 covers the chemical substances used, while section 3.3 focuses on methods used for the singlet oxygen and hydrogen peroxide sample preparation and detection.

3.1 Radiation sources

Gamma
For the gamma irradiation of the samples, the Gammacell 220 Excel from MDS Nordion was used. This self-shielded irradiator uses Co-60 as the source, with a dose rate of approximately 9.1 Gy/min. This rate was calculated according to the displayed information on the Gammacell regarding the activity measured on a specific moment in time. Within the irradiation chamber, the samples were all placed next to each other at the side of the hatch with 1 cm distance from the wall.

X-ray
For the X-ray irradiation, the Phillips MCN 321 tube head was used, paired with a Wolfram anode. The X-ray operated at a voltage of 240 kV, an electric current of 5.0 mA and a FOC of 5.5. The X-ray head was turned towards the floor, hanging 21 cm above the samples (measured from the bottom side of the glass of the X-ray head to the bottom of the irradiated vials). The samples were positioned in such a way that they were all approximately in the centre of the irradiation beam. The dose rate was measured to be approximately 0.65 Gy/min.

3.2 Materials

3.2.1 Nanoparticles

The TiO_2 and ZnO solutions were prepared according to the nanoparticle(mg) to MilliQ water(mL) ratio of 1:2. Thus, the concentration of the nanoparticle stock solutions was 0.5 g/L. The solutions were ultrasonicated for 15 minutes before every use to ensure a homogeneous solution. The solutions should always be handled in flasks wrapped in aluminium foil and in black Eppendorf tubes to avoid light degradation as much as possible.

TiO_2 The titanium(IV) oxide (P-25, CAS 13463-67-7) was manufactured by Degussa. The nanopowder consisted out of a mixture of 85% rutile and 15% anatase. The average particle size was 20 nm, with a purity of 99.9%. The specific surface area was not given by Degussa.

ZnO The zinc oxide (CAS 1314-13-2) was manufactured by Sigma-Aldrich. The average particle size was <50 nm, with a purity of >97%. The particles were doped in 6% Al and had a specific surface area of >10.8 m^2/g.

3.2.2 SOSG

The SOSG probes were obtained in vials of 100 μg each through the manufacturer ThermoFisher. Before using the probes, 33 μL of pure methanol was added per vial, bringing the stock concentration to 5 mM. Previous experiments using SOSG in the same research group were done with SOSG molarities of 10 μM. However, 2 μM of SOSG were used for the experiments conducted for this report. This decision was made after experimentally concluding that 2 μM is already sufficient to make a comparison between the relative amounts of singlet oxygen detected in the TiO_2 and the MilliQ water samples.

3.2.3 List of other chemicals

The other salts and solutions used are given in the list below.

- Acetic acid, manufactured by Sigma-Aldrich (CAS 64-19-7)
- Ammonium heptamolybdate tetrahydrate, manufactured by Merck KGaA (CAS 12054-85-2)
- Hydrogen peroxide (30% w/w), manufactured by Merck KGaA (CAS 7722-84-1)
- Methanol, manufactured by Honeywell (CAS 67-56-1)
- Potassium iodide, manufactured by Merck KGaA (CAS 7681-11-0)

3.3 Methods

3.3.1 Detection of singlet oxygen

Two kinds of samples were prepared for the singlet oxygen detection experiments: a group containing 0.5 mL of the TiO_2 solution (0.5 g/L) + 0.5 mL SOSG probe (2 μM) and a group containing 0.5 mL pure MilliQ water + 0.5 mL SOSG probe. The samples were all prepared in black Eppendorf tubes to block out the light to prevent light degradation of the chemicals and the ROS produced after irradiation. The irradiation itself was either done by exposure to gamma or X-ray using irradiation times that were calculated with the dose rate of the respective radiation source. After this, the samples were centrifuged at 10,000 rpm for 30.0 minutes. The samples were then analysed with the Cary Eclipse Fluorescence Spectrophotometer from Agilent Technologies. For this analysis, it was important to only pipette the supernatant of the samples into the cuvettes of the spectrometer, and thus leaving the nanoparticles behind in the irradiated vial. Furthermore, the emission settings for the analysis are given in the table directly below. For the results, the maximum peak intensity was collected, which was usually present between 524 and 528 nm.

Excitation	504.00 nm
Start	510.00 nm
Stop	600.00 nm
Excitation slit	5.00 nm
Emission slit	10.00 nm

3.3.2 Detection of hydrogen peroxide

Samples consisting out of 1000 μL of the to-be irradiated solutions (either TiO_2 (0.5 g/L), ZnO (0.5 g/L) or MilliQ water) were prepared in black Eppendorf tubes. After irradiation by either the gamma or the X-ray source, the samples were centrifuged at 10,000 rpm for 30.0 minutes. The second part of the sample preparation process for the spectrometry consisted out of pipetting 800 μL of the supernatant of each sample into a new Eppendorf tube. Afterwards, 100 μL of a potassium iodide and 100 μL of a ammonium molybdate stock solution were added to each sample (see the table below for the composition of these stock solutions). The samples were then left to react for 10 minutes, after which they were analysed by the UV-6300PC Double Beam Spectrophotometer with a wavelength measurement region between 200 and 600 nm, a stepcount of 1.0 nm, and a precision of 10. The absorbance values used for the results were obtained by using the absorbance value displayed in the data at exactly 350 nm.

stock name	chemical components
KI solution	2.656 g KI + 16.0 mL MilliQ water
Ammonium molybdate solution	98.9 mg $(NH_4)Mo_7O_{24}\cdot$ 4H_2O + 16.0 mL acetic acid buffer
Acetic acid buffer	976 μL acetic acid + 16.0 mL MilliQ water

4 Results

4.1 Detection of singlet oxygen

A gamma and a low energy X-ray source were used to study the generation of singlet oxygen. The relative amounts of this ROS present in the samples were measured via fluorescence spectroscopy. The output is given in terms of the intensity in arbitrary units (a.u.). Subsection 4.1.1 discusses the results obtained during the gamma irradiation experiments. This is followed by subsection 4.1.2, which discusses the results of the X-ray experiments. Lastly, subsection 4.1.3 gives a comparison between the results of the two irradiation methods for the detection of singlet oxygen.

4.1.1 Gamma irradiation

For the singlet oxygen detection after gamma irradiation, samples of either 0.5 mL MilliQ water or a TiO_2 solution were added to 0.5 mL of the SOSG probe solution (2 μM) before exposure to Co-60. The results thereof are presented in two graphs (Figure 4.1a and Figure 4.1b) as the irradiation and spectrometric analysis were done in two batches. For all doses, except for 0 Gy, three samples were prepared, irradiated, and analysed at the same time. Figure 4.1 shows the mean maximum peak intensity plotted against the dose, with the error bars representing the standard deviation. In this figure, both MilliQ water and TiO_2 exhibit a upward trend, in which the intensity increases over the entire ascending irradiation range. The amount of detected singlet oxygen was generally higher for the TiO_2 samples than for the MilliQ samples irradiated with the same overall dose. The only exception to this was observed at 0 Gy in Figure 4.1a, where the MilliQ water sample showed higher intensity than the respective TiO_2 sample. However, it is important to note that only one background sample was taken for both MilliQ water and TiO_2. These samples therefore do not have any error bars as opposed to the other irradiation groups.

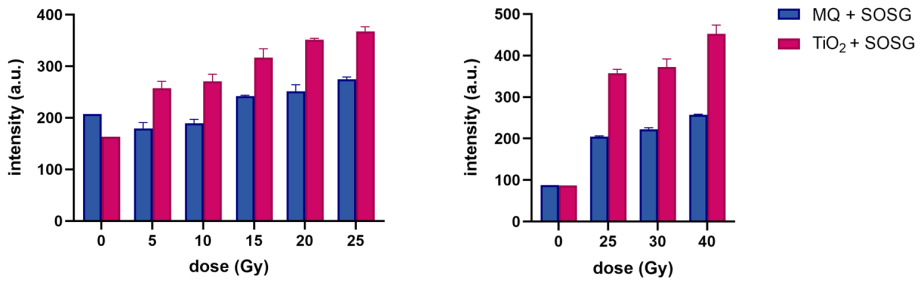

(a) 5 - 25 Gy **(b)** 25 - 40 Gy

Figure 4.1: Singlet oxygen detection: the maximum peak intensity (a.u.) measured by fluorescence spectroscopy for samples consisting of either 0.5 mL TiO_2 (0.5 g/L) solution or MilliQ water, added to 0.5 mL of SOSG probe solution (2 μL). The samples were irradiated with a Co-60 gamma source with doses 5 - 40 Gy in two batches. The error bars represent the standard deviation of the three samples analysed per dose, with 0 Gy being the exception, for which only 1 sample was prepared and analysed.

4.1.2 X-ray irradiation

The same kind of experiment as discussed in subsection 4.1.1 was repeated with an X-ray source instead of a gamma source. The mean maximum peak intensities and the corresponding standard deviations thereof are shown in Figure 4.2. The data is displayed as two separate graphs as the irradiation and analysis of the samples were done in two batches. Both subfigures display an increase for the detected singlet oxygen as the administered dose goes to higher values. Furthermore, TiO_2 exhibits a higher mean intensity for every dose administered, including for 0 Gy. The results of the third batch (30 - 40 Gy) are omitted in this section as the error bars were too large to be able to draw conclusions from the data. However, the graph is given in Figure A.2 as it is mentioned in the discussions section.

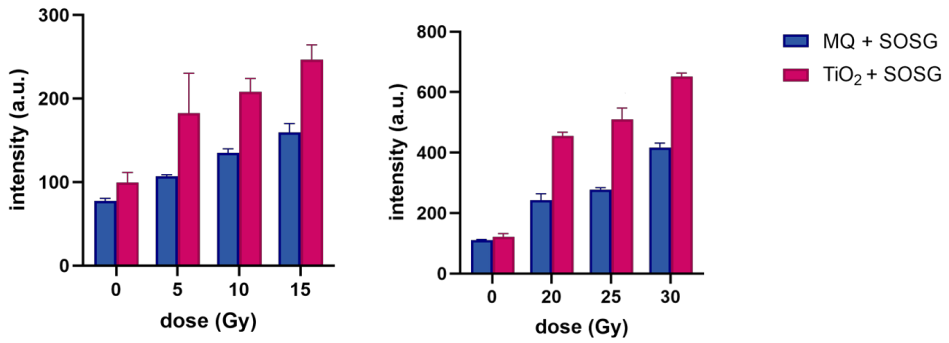

(a) 5 - 15 Gy **(b)** 20 - 30 Gy

Figure 4.2: Singlet oxygen detection: the maximum peak intensity (a.u.) measured by fluorescence spectroscopy for samples consisting of either 0.5 mL TiO_2 (0.5 g/L) solution or MilliQ water, added to 0.5 mL of SOSG probe solution (2 μL). The samples were irradiated with an X-ray source with doses 5 - 30 Gy in two batches. The error bars represent the standard deviation of the 3 samples that were analysed per dose.

4.1.3 Comparison between gamma and X-ray results

Figure 4.3 compares the results obtained for the gamma and X-ray experiments. Due to the varying background intensities of the data from the previous two sections, it was difficult to compare them directly. Therefore, the data had to be scaled. This was done by calculating the ratio of the background samples to the arbitrary value of 100 a.u. The corresponding data sets of the irradiated samples were then scaled according to those ratios, and were then plotted as Figure 4.3. The equivalent unscaled graph is given in Figure A.3. Although the results from this scaling method are not as accurate as they would have been if the experiment was done in one single batch, it can still be used to make a rough comparison. In particular, it shows that X-ray-irradiated samples produced higher intensities than the gamma-irradiated samples when comparing the values at the individual doses. Additionally, the difference between the intensities measured for gamma- and X-ray-irradiated samples is notably larger in the 20 - 30 Gy range than it is for the 5 - 15 Gy.

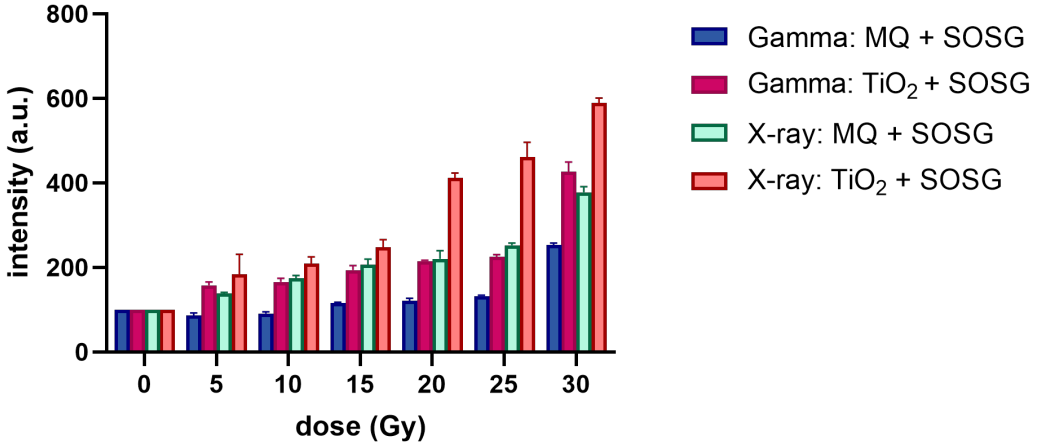

Figure 4.3: Singlet oxygen detection: comparison between the data sets of X-ray and gamma irradiated samples (range 5 - 30 Gy) consisting of either 0.5 mL TiO_2 (0.5 g/L) solution or MilliQ water, added to 0.5 mL of SOSG probe solution (2 μL). All data points were adjusted according to the ratio of the mean background intensity to the arbitrary value of 100 a.u.. The error bars represent the standard deviation of the intensities measured during fluorescence spectroscopy.

4.2 Detection of hydrogen peroxide

The same experiments as described in subsection 4.1.1 were carried out to detect hydrogen peroxide, this time with an UV-VIS spectrometer to detect this other kind of ROS. An important change was that these experiments were done with ZnO instead of TiO_2 at first, as it has been observed during previous studies that TiO_2 can decompose hydrogen peroxide at its surface [10]. subsection 4.2.1 covers the results of irradiating ZnO and MilliQ water samples with a gamma source. Whereas subsection 4.2.2 focuses on the results obtained with the same procedure but with X-ray irradiation instead. This is followed by subsection 4.2.3, where the two data sets from subsection 4.2.1 and subsection 4.2.2 are compared to one another. Lastly, subsection 4.2.4 discusses the results from simultaneously irradiating TiO_2 and ZnO samples with a Co-60 gamma source. The output of the UV-VIS spectrometer was given in the form of the absorbance (a.u.). These values were then converted to the H_2O_2 (μM) molarity using a calibration curve for these specific experiments and the spectrometer used (Figure A.1). All graphs in the following sections display the results in terms of this molarity, whereas the graphs with the original intensity values are given in the appendix (Figure A.4 to Figure A.9).

4.2.1 Gamma irradiation of MilliQ water and ZnO samples

Firstly, the natural ability of water to produce H_2O_2 was investigated by irradiating samples containing 100% MilliQ water. The results thereof are shown in Figure 4.4, for which the molarity of the samples was obtained by converting the absorbances measured via UV-VIS spectrometry according to the calibration curve shown in Figure A.1. The concentration of H_2O_2 detected for these MilliQ water samples increased as the dose got higher.

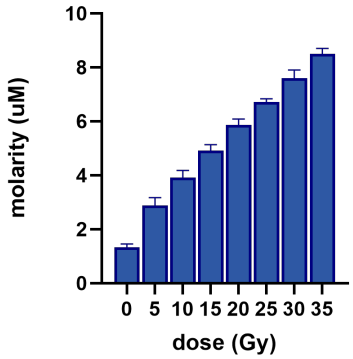

Figure 4.4: Hydrogen peroxide detection: H_2O_2 molarity (μM) measured by UV-VIS spectroscopy for samples consisting out of 800 μL MilliQ water, with 100 μL potassium iodide and 100 μL ammonium molybdate stock solutions added between irradiation and the spectroscopic analysis. The samples were irradiated with a Co-60 gamma source with doses of 5 - 35 Gy. The error bar represent the the standard deviation of the 3 samples that were analysed per dose. The equivalent absorbance graph is shown in Figure A.4.

Figure 4.5 shows the results of irradiating ZnO samples while using the same procedure. The irradiation and analysis of the samples were done in two batches. Hence, the splitting of the data into two graphs. Both Figure A.5a and Figure A.5b exhibit an upward trend where the H_2O_2 molarity increases as more radiation is administered to the samples. As for the displayed data itself, the mean molarity of all ZnO samples, including 0 Gy, is significantly higher than those of the MilliQ water samples shown in Figure 4.4. Furthermore, the uncertainties shown in Figure 4.5 are more significant than those observed for the equivalent experiment with the MilliQ water samples.

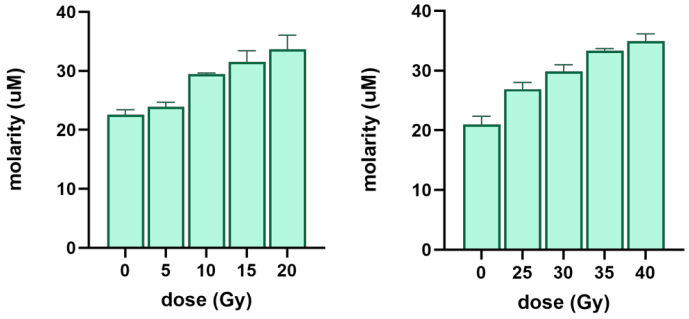

(a) 5 - 20 Gy **(b)** 25 - 40 Gy

Figure 4.5: Hydrogen peroxide detection: H_2O_2 molarity (μM) measured by UV-VIS spectroscopy for samples consisting out of 800 μL ZnO solution (0.5 g/L), with 100 μL potassium iodide and 100 μL ammonium molybdate stock solutions added between irradiation and the spectroscopic analysis. The samples were irradiated with a Co-60 gamma source with doses 5 - 40 Gy in two batches. The error bars represent the standard deviation of the 3 samples that were analysed per dose. The equivalent absorbance graphs are shown in Figure A.5.

4.2.2 X-ray irradiation of MilliQ water and ZnO samples

The same kind of experiment as discussed in subsection 4.2.1 was repeated with an X-ray source instead of a gamma source. The mean H_2O_2 molarity measured in the MilliQ water samples, and the corresponding standard deviations thereof, are shown in Figure 4.6a and Figure 4.6b. The data follows a linear trend in both of these sub-graphs. It is not immediately clear whether this trend is continuous between the two due to the different y-axis scales and the varying background values. However, the slopes of the fitted linear trend are almost identical (0.3176 μM H_2O_2 per Gy for Figure 4.6a and 0.3173 μM H_2O_2 per Gy for Figure 4.6b). Thus the molarity detected in the sample increases roughly the same amount every time the dose is increased by 5 Gy. The plots showing these linear regressions and their corresponding R^2 values are given in Figure A.7.

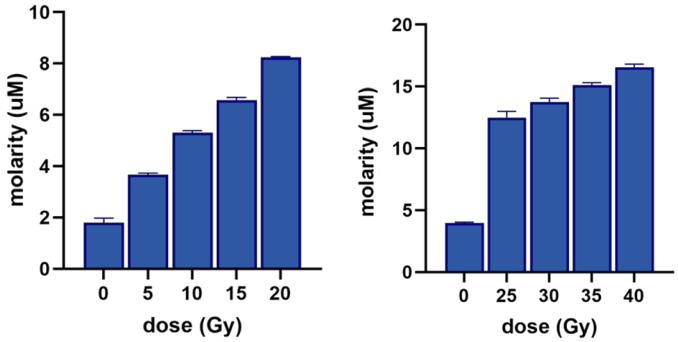

(a) 5 - 20 Gy **(b)** 25 - 40 Gy

Figure 4.6: Hydrogen peroxide detection: H_2O_2 molarity (μM) measured by UV-VIS spectroscopy for samples consisting out of 800 μL MilliQ water, with 100 μL potassium iodide and 100 μL ammonium molybdate stock solutions added between irradiation and the spectroscopic analysis. The samples were irradiated with an X-ray source with doses 5 - 40 Gy in two batches. The error bars represent the standard deviation of the three samples that were analysed per dose. The equivalent absorbance graphs are shown in Figure A.6.

The results from irradiating the ZnO samples with the X-ray source are given in Figure 4.7. The samples were centrifuged and analysed per dose immediately after their irradiation, as the irradiation times varied between approximately 7 minutes for 5 Gy to 61 minutes for 40 Gy. Because of this, three ZnO background samples (0 Gy) were analysed alongside each batch of irradiated samples. The absorbance values of these background measurements varied significantly between the different batches, making a direct comparison impossible. Therefore, the mean of the three background samples was calculated and then subtracted from the respective absorbance values of the corresponding irradiated samples. The mean absorbances displayed in Figure A.8 and the mean molarities in Figure 4.7 are the results of this method.

The X-ray experiment for ZnO took place over two days, with the first group being the samples from 5 to 25 Gy and the second one from 30 to 40 Gy. For the first group, the average absorbance of the 15 Gy sample was below the 0 Gy mean value due to a systematic error occurring during the preparation of these samples. Therefore, a new set of vials was prepared and irradiated for that dose on the second day, which could have caused the elevated absorbance in Figure 4.7 and Figure A.8. As was observed for the previous graphs in this chapter, the H_2O_2 molarity detected increased as the dose increased as well. Besides this, the molarity values were below the ones observed for MilliQ water in Figure 4.6 when the differences in background concentration are not considered.

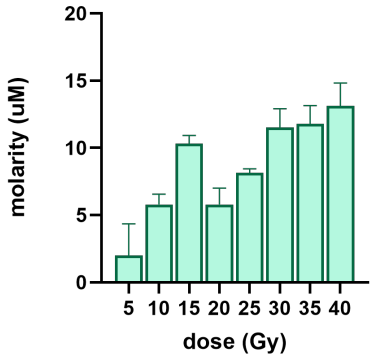

Figure 4.7: Hydrogen peroxide detection: H_2O_2 molarity (μM) measured by UV-VIS spectroscopy for samples consisting out of 800 μL ZnO solution, with 100 μL potassium iodide and 100 μL ammonium molybdate stock solutions added between irradiation and the spectroscopic analysis. The samples were irradiated with an X-ray source with doses of 5 - 40 Gy. The displayed values are the means of the molarity values per dose with the mean background H_2O_2 molarity (0 Gy) subtracted from them. The error bars represent the standard deviation, and the equivalent absorbance graph is shown in Figure A.8.

4.2.3 Comparison between gamma and X-ray results

Figure 4.8 compares the results obtained for the gamma and X-ray experiments for the MilliQ water and the ZnO solution separately. A direct comparison between the data sets in section 4.2 was not possible as they all had strongly varying background molarities. Therefore, as was done for Figure 4.7, the mean background H_2O_2 molarity (0 Gy) was subtracted from the respective concentrations measured for the irradiated samples. This method is not entirely suited to even out the jumps in values observed between adjacent data where the graphs were merged, which is especially noticeable in Figure 4.8b. Nonetheless, a rough comparison can be made. For the MilliQ water samples, the H_2O_2 molarities detected during the X-ray experiments are consistently higher than the values measured during the gamma experiments. The difference in molarities between these two methods seems to get larger as the dose increases. On the other hand, Figure 4.8b does not exhibit a clear trend, partly due to the discrepancy between the two merged gamma batches, as mentioned earlier. The mean molarity of the irradiated X-ray samples is not always higher than the mean of the gamma samples anymore. Additionally, the difference between the mean molarities does not seem to get larger, as the dose increases as was observed in Figure 4.8a.

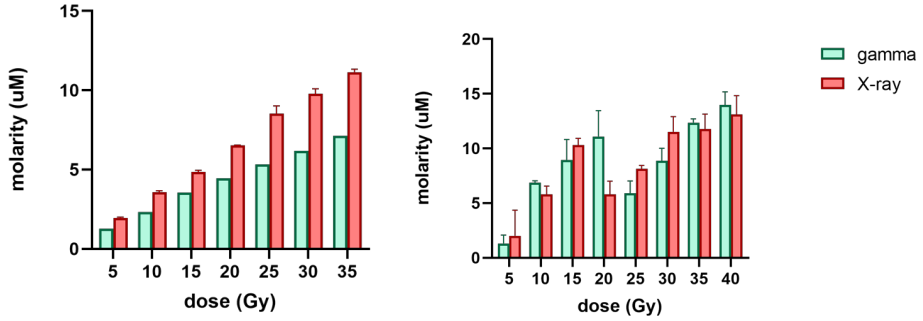

(a) MilliQ water samples **(b)** ZnO samples

Figure 4.8: Hydrogen peroxide detection: comparison between the data sets of X-ray and gamma irradiated samples for the H_2O_2 molarity (μM) detection in UV-Vis spectroscopy. The samples consisted of (a) 800 μL MilliQ water or (b) 800 μL ZnO solution, with 100 μL potassium iodide and 100 μL ammonium molybdate stock solutions added between irradiation and the spectroscopic analysis. The irradiation range is 5 - 40 Gy. Furthermore, the displayed values are the means of the molarity values per dose that had the mean background H_2O_2 molarity (0 Gy) subtracted from them. The error bars represent the standard deviation.

4.2.4 Gamma irradiation of TiO_2 samples compared to ZnO samples

The ability of TiO_2 to produce hydrogen peroxide under ionising radiation was investigated by exposing these solvated nanoparticles to the Co-60 gamma source. This was done for a range from 5 to 40 Gy in three batches, as is shown in Figure 4.9. For each dose, three TiO_2 samples were simultaneously irradiated alongside three ZnO samples to be able to compare the detected H_2O_2 molarities of the two different nanoparticles. The mean concentrations for ZnO are increasing with roughly the same trend as was observed in Figure 4.5, which is in accordance with the results of section subsection 4.2.1. The only inconsistency is the molarity measured at 30 Gy, which is lower than the one measured at 25 Gy. However, the measurements at 40 Gy indicate that the concentration H_2O_2 does not stagnate or decline past 35 Gy.

Furthermore, the exact molarity values for ZnO do not significantly differ from those displayed in Figure 4.5. For TiO_2 on the other hand, there is not such a pronounced upward trend. The peak height is relatively stagnant at around 10 μM throughout the entire irradiation range, with the higher irradiation doses seeming to have a slightly elevated mean for the detected H_2O_2 molarity as compared to the lower doses. Additionally, the measured H_2O_2 molarity of the TiO_2 is constantly lower than the one of ZnO, including for the 0 Gy background samples.

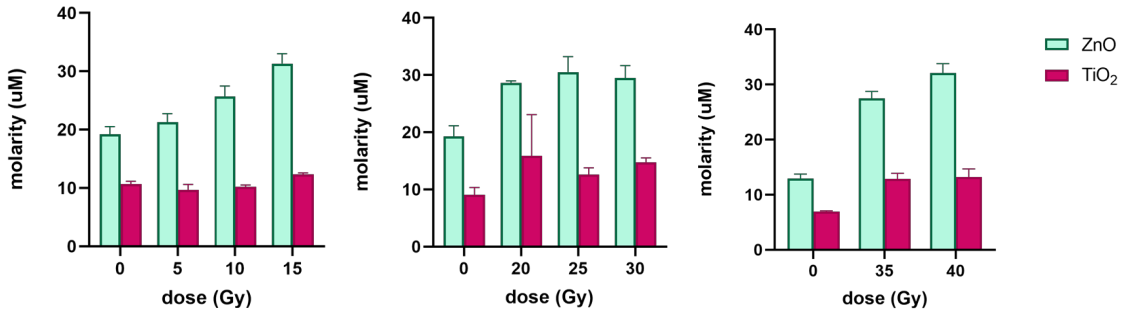

(a) 5 - 15 Gy **(b)** 20 - 30 Gy **(c)** 35 - 40 Gy

Figure 4.9: Hydrogen peroxide detection: H_2O_2 molarity (μM) measured by UV-VIS spectroscopy for samples consisting of 800 μL of either a TiO_2 or a ZnO solution (0.5 g/L), with 100 μL potassium iodide and 100 μL ammonium molybdate stock solutions added between irradiation and the spectroscopic analysis. The samples were irradiated with a Co-60 gamma source with doses in the range 5 - 40 Gy in three batches. The error bars represent the standard deviation of the 3 samples that were analysed per dose. The equivalent absorbance graphs are shown in Figure A.9.

5 Discussion

5.1 Formation of singlet oxygen by TiO_2 under gamma and X-ray irradiation

5.1.1 Comparison between the singlet oxygen production for TiO_2 and MilliQ

The results discussed in subsection 4.1.1 and subsection 4.1.2 yield some promising results for the use of TiO_2 nanoparticles in radiotherapy. TiO_2 seems to produce more singlet oxygen when irradiated by either a gamma or an X-ray source than is generated through the radiolysis of water. The only exception to this was observed for the gamma 0 Gy sample in Figure 4.2. However, as only one MilliQ water and one TiO_2 sample were analysed, no firm conclusions can be drawn from this. For the X-ray samples, it seemed like more singlet oxygen was present in the TiO_2 background samples than in those with MilliQ water. In response to this, two t-tests were performed for the 0 Gy samples in both Figure 4.2a and Figure 4.2b. This was possible for these samples as the measurements were repeated 3 times for both TiO_2 and MilliQ water, as compared to the single measurements for the gamma background samples. The difference between the intensity values for Figure 4.2b was negligibly small, whereas the t-test for Figure 4.2a came back as statistically significant. This is unexpected, as TiO_2 functions as a photosensitizer and should thus only be activated when exposed to light/radiation, as has also been reported in previous papers [46]. Therefore, it would be good to repeat the 0 Gy measurement to probe whether this significant difference will occur again under the same experimental conditions. As for the irradiated samples, the results in Figure 4.1 and Figure 4.2 showed that, despite the varying sizes of the error bars, an increase in the amount of applied radiation will yield an increase in the formation of singlet oxygen over the researched radiation range for both compounds. Lastly, the results of the 30 - 40 Gy irradiated X-ray samples were left out of the report due to the large error bars. These were especially evident for the MilliQ water, while the TiO_2 samples showed a relatively stagnant trend instead when the dose increased. These unexpected results were exclusively observed for the 30 and 40 Gy samples, which were the only samples that were ultrasonicated before irradiation. This phenomenon has been observed before for distilled water, where the fluorescence intensity of the SOSG probe increased greatly in response to ultrasound [47]. Therefore, samples containing SOSG should not be ultrasonicated during any stage in future experiments.

5.1.2 Comparison between singlet oxygen formation under gamma and X-ray irradiation

Both X-ray and gamma irradiation were used to study the effects of ROS formation on TiO_2 nanoparticles. Whereas subsection 4.1.1 and subsection 4.1.2 displayed the results of these two irradiation sources individually, subsection 4.1.3 made a direct comparison. Herein, it was observed that although the same overall doses were applied during the gamma and X-ray irradiation, the resulting intensities measured by the fluorescence spectrometer were noticeably different. Namely, for each dose, more singlet oxygen was detected for samples irradiated by X-rays than for those irradiated by the gamma source. This difference in singlet oxygen detection became more significant the more the dose increased. As a higher intensity corresponds to elevated levels of singlet oxygen, it seems like TiO_2 can produce more of this ROS when interacting with X-rays than with gamma radiation. One of the key differences between these two types of irradiation was the energy of the photons. The X-rays which were used in this experiment had a energy in the magnitude

of keV, whereas Co-60 generates gamma radiation with an energy between approximately 1.1 and 1.3 MeV [48]. Hence, lower energies seem to have a better interaction with the nanoparticles, which in turn causes an increase in the singlet oxygen concentration measured in the solution. It is, however, important to repeat this experiment with fewer variables to be able to draw any firm conclusions. For instance, the irradiation times varied greatly between the X-ray and gamma samples.

5.2 Formation of hydrogen peroxide by ZnO under gamma and X-ray irradiation

5.2.1 Comparison between hydrogen peroxide production for ZnO and MilliQ

.

The samples consisting of pure MilliQ water were able to raise the hydrogen peroxide concentrations as the applied dose got higher for both the gamma and X-ray experiments. Therefore, radiolysis is successful in generating increasing amounts of this ROS in response to radiation to at least 40 Gy. These results agree with previous research, where these trends were observed as well for the H_2O_2 generation in distilled water during similar experiments [49]. The ZnO solutions also showed an increase in the produced amount of H_2O_2 in response to higher doses of radiation. This more or less gradual increase in the formation of this ROS is likely linked to a response in one of the mechanisms concerning the electron-hole pairs. For example, it could be due to an increase in the generation of these charge carriers, or to a lower recombination rate. The same explanation probably applies to TiO_2 as well, as both nanoparticles are semiconductors with approximately the same band gap energy.

Samples containing ZnO nanoparticles seemed to be able to produce more H_2O_2 than the pure MilliQ water samples when exposed to the gamma source. This indicates that the use of ZnO, and therefore TiO_2 likely as well, could aid gamma radiotherapy by generating elevated levels of this ROS. The differences in the H_2O_2 molarity detected between the MilliQ water and the ZnO solution were much less noticeable for the X-ray experiments. Especially for the higher doses, the differences in molarity between the MilliQ water and ZnO samples were mostly insignificant according to the t-test. Thus, it seems like ZnO cannot increase the H_2O_2 molarity in the surrounding solution more than radiolysis is able to do. It is, however, important to consider the large variance in the error bars for the ZnO samples as compared to the MilliQ water standard deviation. This relatively high uncertainty can be linked to the method used to prepare the samples for the UV-VIS analysis. Unlike for the fluorescence measurements, two stock solutions had to be added between the irradiation of the samples and the analysis with the spectrometer. These three solutions had to be mixed to ensure that the final composition was homogeneous for the reaction to fully take place. It was important that as few nanoparticles as possible were in this final solution, as they could interfere with the H_2O_2 detection process by causing elevated and imprecise absorbance values.

To avoid this problem, a method was developed to ensure that the majority of the nanoparticles were not transferred from the irradiated vials to the new vials for the UV-VIS analysis. With this method, samples with volumes of 1000 μL of the nanoparticle solutions were created pre-irradiation, instead of the 800 μL that were previously used. Before doing so, a small experiment was conducted to verify that for these small amounts of solution, no significant difference was observed for the amount of H_2O_2 generated per mL. Then, after irradiating and centrifuging the samples, 800 μL of the supernatant was taken out of the irradiated vials and put into the new ones. Next, the two stock solutions were added, and the new solution was mixed and left to react for 10 minutes. This method was partly successful in ensuring that most of the nanoparticles stayed behind in the irradiated vial. When using clear vials, it could be seen that a large fraction of the nanoparticles were precipitated alongside the wall of the Eppendorf tube and were not sucked up when pipetting out the 800 μL of the supernatant. Despite this, the solution was still relatively cloudy after being centrifuged, as can be seen in Figure 5.1. Thus, the supernatant that was transferred to the new vials likely contained a significant amount of nanoparticles. As the precipitation pattern was different for each vial, the exact amount that was transferred could have varied a lot per sample. This could have resulted in the large fluctuations of the measured absorption during the UV-VIS spectrometric analysis.

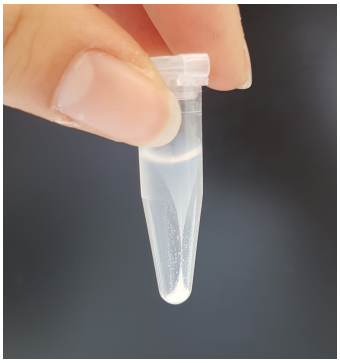

Figure 5.1: Eppendorf tube for the detection of hydrogen peroxide immediately after being centrifuged for 30 minutes at 10,000 rpm. The solution was still relatively cloudy, meaning that a large fraction of the nanoparticles was not precipitated.

5.2.2 Comparison between hydrogen peroxide formation for ZnO and MilliQ water under gamma and X-ray irradiation

Figure 4.8a shows the H_2O_2 molarities that were detected while analysing the MilliQ water samples with a UV-VIS spectrometer after both X-ray and gamma irradiation. The X-ray samples all seem to have generated higher levels of H_2O_2 as compared to those of gamma. Additionally, the difference in molarities of the two radiation sources increased with the doses. In Figure 4.8b on the other hand, there is no such clear trend visible. The X-ray samples do not consistently have higher H_2O_2 molarities than those exposed to the gamma source. The t-test even marks the differences in mean values of the gamma and X-ray samples as insignificant for the majority of the doses. One factor that makes it difficult to accurately compare the X-ray and gamma results is the large error bars. These large variances have been attributed to the UV-VIS samples containing a significant amount of nanoparticles. However, another important factor for this might have been the instability of the formed H_2O_2, which may have been the reason for the discrepancy in Figure 4.7. Despite the samples all being prepared at the same time, the absorbances of the second batch (which included the samples used for the 15 Gy measurement) were notably higher. This could thus hint that the experimental procedure is prone to environmental factors, such as photodecomposition. Clear Eppendorf tubes were used for certain parts of the hydrogen peroxide experiments due to delayed supply deliveries. Although the samples were kept in the dark as much as possible, some light degradation might have taken place with varying effects as H_2O_2 is relatively light-sensitive [50]. Additionally, H_2O_2 has been found to decompose in a temperature range starting at 15 °C [51]. Therefore the way of handling the samples for these experiments could potentially yield significant differences in the measured absorbances and molarities. For future research, it would therefore be recommended to irradiate and analyse all samples in one batch. Additionally, it would be beneficial to repeat the H_2O_2 detection experiments with ZnO to gain a better insight as to whether the energy of the ionising radiation does or does not make a difference in the concentration of H_2O_2 being produced.

5.3 Generation of hydrogen peroxide by TiO_2

The last part of the results section covered the H_2O_2 molarities measured for the supernatant of both a ZnO and a TiO_2 solution. The irradiation was done by the Co-60 gamma source and the results are shown in Figure 4.9. For ZnO, both the trend and the mean H_2O_2 molarity values were in line with the previous experiment in which these nanoparticles were exposed to gamma radiation. The TiO_2 particles, however, did not exhibit this clear upward trend. Namely, the detected H_2O_2 molarities seemed to be relatively stagnant around 10 μM. Nevertheless, there was a very slight increase in the H_2O_2 concentration when going to higher doses, which was labelled as significant according to the t-test. The slope of this trend was nevertheless notably smaller than the one observed for the ZnO samples.

Given the similar semiconductor characteristics of ZnO and TiO_2, it is unexpected that significantly less H_2O_2 is detected in the TiO_2 samples as opposed to the ZnO samples. Previous studies also observed that there was no real increase in the amount of H_2O_2 detected in TiO_2 samples after irradiation. Shabel et al. concluded in one of their studies regarding this that the swift decomposition of H_2O_2 on TiOs's surface by oxidation or reduction reactions makes it difficult to detect and quantify the amount of H_2O_2 produced. Furthermore, the TiO_2 particles used in the experiments for this thesis consisted of 85% rutile and 15% anatase. The relatively large share of rutile could have aided the decomposition of H_2O_2 as this polymorph has been found to degrade this ROS more readily than the other chemical structures. This property is mainly attributed to the reduction of hydrogen peroxide being much more energetically favourable for rutile due to the energy levels of its conduction band. For anatase on the other hand, the reduction of oxygen and the reduction of hydrogen peroxide are both in competition with one another [10].

Although TiO_2 could decompose H_2O_2 to H_2O or O2 and H^+, it might also be possible that this semiconductor converts hydrogen peroxide to other chemical species. As is shown in Figure 2.4, H_2O_2 could be directly converted to hydroxyl or superoxide radicals under irradiation. These compounds could then also be further converted from, for example, superoxide radicals to singlet oxygen by oxidation. These conversions could take place so rapidly that almost none of the generated H_2O_2 is detected by UV-VIS. To verify whether these mechanisms are at play, a new set of experiments needs to be designed. These experiments could consist of blocking all but one reaction path to detect whether the concentration of the corresponding product is affected. Another possibility might be that TiO_2 adsorbs the H_2O_2 to its surface. After irradiation, the samples were transported back to the lab and centrifuged for 30 minutes. As there was no to very little irradiation of the samples during this time, TiO_2 should not have been activated as it acts as a photosensitizer. It might however have been possible that the nanoparticles did adsorb some of the H_2O_2 molecules to their surfaces without converting or degrading this ROS. If this did indeed occur, then the nanoparticles with the adsorbed H_2O_2 would have been mostly precipitate after the centrifugation process, causing them to not be transferred into the cuvettes for the UV-VIS analysis.

In short, the cause behind the low H_2O_2 molarity values measured for the TiO_2 samples is unknown. It might be due to the decomposition, conversion, or adsorption of this ROS in the presence of TiO_2. More research should be conducted to discover what mechanism is mainly at play and what factors influence this process. Until then, it is not possible to draw any final conclusions as to whether TiO_2 has the potential to increase the hydrogen peroxide levels in its surrounding solution in response to interaction with ionising radiation.

6 Conclusion and Recommendations

6.1 Conclusions

The goal of this report was to analyse the ability of TiO_2 to produce singlet oxygen and hydrogen peroxide in response to ionising radiation. The results thereof were compared to those obtained from MilliQ water samples, in which ROS are formed through radiolysis, as well as in part to those from ZnO. For the detection of singlet oxygen and hydrogen peroxide, fluorescence and UV-VIS spectrometry were used respectively. The irradiation itself was achieved by exposure to either a Co-60 gamma or a low-energetic X-ray source over a range of 5 to 40 Gy. Based on these experiments, the following conclusions can be drawn:

- Both the TiO_2 and MilliQ water samples showed an increase in the concentration of produced singlet oxygen as the received radiation dose increased. This effect was observed over the entire irradiation range. Furthermore, the mean maximum intensities of the fluorescence spectra peaks for the irradiated TiO_2 solutions were significantly higher than those for MilliQ water. Both chemical compounds are therefore able to produce this ROS under the two types of ionising radiation, but with the TiO_2 samples generating more singlet oxygen than the radiolysis of water does under the specific experimental conditions that were imposed.

- For the hydrogen peroxide detection experiments, similar trends as described above were observed for the irradiation of ZnO and MilliQ water samples. Both of these compounds showed an increase for the detected amount of H_2O_2 when the applied dose increased. Additionally, samples containing ZnO nanoparticles seemed to be able to produce more H_2O_2 than the pure MilliQ water samples when exposed to the Co-60 gamma source. For the X-ray irradiation, this difference in H_2O_2 concentrations between the MilliQ water and the ZnO samples was much less noticeable, with often no significant difference, especially for the higher irradiation doses.

- For the singlet oxygen experiments, it was observed that for the same overall dose, more of this ROS was detected in the X-ray samples than in those irradiated by the gamma source for the same chemical species. This phenomenon occurred for the formation of H_2O_2 in pure MilliQ water samples as well. These results are likely attributed to the lower energy of the X-ray radiation (keV) as compared to the MeV energies of the gamma radiation. For the ZnO samples, no significant difference was observed for the detected H_2O_2 concentrations between the two irradiation methods.

- Both TiO_2 and ZnO were simultaneously irradiated and analysed to make a comparison between the two regarding their abilities to produce hydrogen peroxide. It was observed that TiO_2 produced significantly less of this ROS over the entire irradiation range. Furthermore, the trend with which the H_2O_2 was detected, was much less steep than the one observed for ZnO. Potential causes for this behaviour of TiO_2 might be attributed to either decomposition, conversion, or adsorption of H_2O_2 at the surface of TiO_2. Although this effect seemed to be much more prominent for TiO_2 than for ZnO, it might still occur for the latter as well.

To conclude, TiO_2 seemed to be successful in generating elevated levels of singlet oxygen under exposure to X-ray and gamma irradiation, which exceeded the concentrations produced by the radiolysis of water. This is promising for the future of this semiconducting nanoparticle as a photosensitizer in radiotherapy. Nonetheless, TiO_2 could not raise the H_2O_2 levels in the solution to the same degree as ZnO was able to do

when irradiated by Co-60. It is therefore important to look further into the underlying mechanisms to fully understand the pathways along which TiO_2 can produce these ROS and how the corresponding processes are influenced by environmental factors and each other.

6.2 Recommendations

For future research, the following recommendations are given:

- As discussed previously, it has been observed for both TiO_2 and MilliQ water samples, that X-rays are able to produce higher amounts of singlet oxygen than gamma irradiation. This phenomenon was also observed for the H_2O_2 production by MilliQ water, and is likely caused by the difference in energy of the photons of the two radiation sources. It is therefore recommended that a new set of experiments is designed to be able to more thoroughly investigate the effect of the radiation energy on the formation of singlet oxygen, hydrogen peroxide and possibly other ROS for a variety of chemical compounds (including TiO_2, ZnO, and MilliQ water). When doing this, it is important that only the energy of the radiation is a variable. The irradiation time for example, should be equal for all samples unlike the experiments performed in this report.

- The effects of certain metal and non-metal dopants on the photocatalytic properties of TiO_2 and ZnO could be tested. For example, compounds that could be grafted to the surface of the nanoparticles are transition metals containing organic ligands. Different studies on surface functionalization of TiO_2 have already demonstrated that it is possible to improve light absorption with this technique [7], and could thus possibly influence the ROS production rate and other characteristics of TiO_2.

- As much remains unknown regarding the ROS-producing mechanisms of TiO_2, it would be valuable to develop new experiments to study these. Firstly, it might be beneficial to repeat similar experiments for the detection of other ROS, e.g. hydroxyl and superoxide radicals, as well. Moreover, it was concluded that TiO_2 might adsorb, convert or degrade H_2O_2 at its surface, causing little to no elevated levels of this ROS in the surrounding solution. To test whether TiO_2 is able to convert, for example, H_2O_2 into $^1O_2$, all conversion pathways except for this one should be blocked by using scavengers among other methods.

- It is recommended to develop a new method for separating the nanoparticles from the supernatant. A recent experiment at TU Delft proved to be more successful in separating the two by using a 0.22 μm membrane filter. Finding the most suited method to separate the nanoparticles from the solution would enable us to obtain a more accurate analysis of the ROS quantities present in the solutions.

- For TiO_2, the majority of studies on its ROS-generating abilities were conducted with the rutile or anatase polymorph, or a combination of both. As was mentioned in subsection 2.3.4, brookite might be able to produce as many, or possibly more, ROS than both other TiO_2 configurations. For that reason, the singlet oxygen and hydrogen peroxide detection experiments could be repeated for all configurations. By doing so, it is possible to gain a better insight into which polymorph is most suited for the use in radiotherapy, and what the characteristic properties are for each of them regarding their semiconductor behaviours.

Bibliography

[1] Tadeusz Dyba, Giorgia Randi, Freddie Bray, Carmen Martos, Francesco Giusti, Nicholas Nicholson, Anna Gavin, Manuela Flego, Luciana Neamtiu, Nadya Dimitrova, Raquel Negrão Carvalho, Jacques Ferlay, and Manola Bettio. The european cancer burden in 2020: Incidence and mortality estimates for 40 countries and 25 major cancers. *European Journal of Cancer*, 157:308–347, 11 2021.

[2] Hyuna Sung, Jacques Ferlay, Rebecca L Siegel, Mathieu Laversanne, Isabelle Soerjomataram, Ahmedin Jemal, and Freddie Bray. Global cancer statistics 2020: Globocan estimates of incidence and mortality worldwide for 36 cancers in 185 countries. *CA: a cancer journal for clinicians*, 71:209–249, 2021.

[3] Rajamanickam Baskar, Kuo Ann Lee, Richard Yeo, and Kheng-Wei Yeoh. Cancer and radiation therapy: Current advances and future directions. *International Journal of Medical Sciences*, 9:193–199, 2012.

[4] Xingchen Peng, Zhigong Wei, and Leo E Gerweck. Making radiation therapy more effective in the era of precision medicine. *Precision Clinical Medicine*, 3:272–283, 12 2020.

[5] Helen H.W. Chen and Macus Tien Kuo. Improving radiotherapy in cancer treatment: Promises and challenges. *Oncotarget*, 8:62742–62758, 9 2017.

[6] Deep Kwatra, Anand Venugopal, and Shrikant Anant. Nanoparticles in radiation therapy: a summary of various approaches to enhance radiosensitization in cancer. *Translational Cancer Research*, 2(4), 2013.

[7] Titanium dioxide nanoparticles: Prospects and applications in medicine. *Nanomaterials*, 10:387, 2 2020.

[8] Ruth Edge and T. George Truscott. The reactive oxygen species singlet oxygen, hydroxy radicals, and the superoxide radical anion—examples of their roles in biology and medicine. *Oxygen*, 1:77–95, 10 2021.

[9] M.M. de Jong. An investigation in the production of singlet oxygen by titanium dioxide nanoparticles under ionizing photon radiation, 3 2021.

[10] K. Sahel, L. Elsellami, I. Mirali, F. Dappozze, M. Bouhent, and C. Guillard. Hydrogen peroxide and photocatalysis. *Applied Catalysis B: Environmental*, 188:106–112, 7 2016.

[11] Hellmut Fritzsche and Melba Phillips. Electromagnetic radiation. *Encyclopedia Britannica*, 7 2020.

[12] Juliana H. J. Mortenson. The fundamental physics of electromagnetic waves, 6 2011.

[13] Kishor Mehta. Radiation: Basic principles. *Journal of Vascular Surgery*, 42:1237–1238, 12 2005.

[14] Daniel Bell and Nicholas Parry. Electron capture, 5 2020.

[15] Glenn Stark. Gamma ray. *Encyclopedia Britannica*, 10 2021.

[16] Perry Sprawls. *The Physical Prinicples of Medical Imaging*. Aspen Publishers, 2 edition, 1993.

[17] Ping Xia and Andrew Godley. *Physics in Radiation Oncology Self-Assessment Guide*. Demos Medical Publishing, 1 edition, 2016.

[18] Hasan Murshed. *Fundamentals of Radiation Oncology*. Elsevier, 2019.

[19] Almahdi Mousa, Kus Kusminarto, and Gede Bayu Suparta. A new simple method to measure the x-ray linear attenuation coefficients of materials using micro-digital radiography machine. *International Journal of Applied Engineering Research*, 12:10589–10594, 2017.

[20] Seyed Hossein Hassanpour and Mohammadamin Dehghani. Review of cancer from perspective of molecular. *Journal of Cancer Research and Practice*, 4:127–129, 12 2017.

[21] Jehad F. Alhmoud, John F. Woolley, Ala-Eddin Al Moustafa, and Mohammed Imad Malki. Dna damage/repair management in cancers. *Cancers*, 12:1050, 4 2020.

[22] Sibaji Sarkar, Garrick Horn, Kimberly Moulton, Anuja Oza, Shannon Byler, Shannon Kokolus, and McKenna Longacre. Cancer development, progression, and therapy: An epigenetic overview. *International Journal of Molecular Sciences*, 14:21087–21113, 10 2013.

[23] Damien Féron, editor. *Nuclear Corrosion Science and Engineering*. Woodhead Publishing, 1st edition, 2012.

[24] Sophie Le Caër. Water radiolysis: Influence of oxide surfaces on h2 production under ionizing radiation. *Water*, 3:235–253, 2 2011.

[25] Upadhyayula Sai Srinivas, Bryce W.Q. Tan, Balamurugan A. Vellayappan, and Anand D. Jeyasekharan. Ros and the dna damage response in cancer. *Redox Biology*, 25:101084, 7 2019.

[26] Zhengzhi Zou, Haocai Chang, Haolong Li, and Songmao Wang. Induction of reactive oxygen species: an emerging approach for cancer therapy. *Apoptosis*, 22:1321–1335, 11 2017.

[27] Alex Senchenkov and Steven L. Moran. Merkel cell carcinoma. *Plastic and Reconstructive Surgery*, 131:771e–778e, 5 2013.

[28] Myriam Laprise-Pelletier, Teresa Simão, and Marc-André Fortin. Gold nanoparticles in radiotherapy and recent progress in nanobrachytherapy. *Advanced Healthcare Materials*, 7:1701460, 8 2018.

[29] Professor Erno Sajo. *Nanoparticle Enhanced Radiation Therapy*. IOP Publishing Ltd, 2020.

[30] Esho Qasho Youkhana, Bryce Feltis, Anton Blencowe, and Moshi Geso. Titanium dioxide nanoparticles as radiosensitisers: An in vitro and phantom-based study. *International Journal of Medical Sciences*, 14:602–614, 2017.

[31] Yidan Wang, Allan Sauvat, Celine Lacrouts, Jérôme Lebeau, Romain Grall, Marie Hullo, Fabrice Nesslany, and Sylvie Chevillard. Tio2 nanomaterials non-controlled contamination could be hazardous for normal cells located in the field of radiotherapy. *International Journal of Molecular Sciences*, 21:940, 1 2020.

[32] Kenichi Ozawa, Masato Emori, Susumu Yamamoto, Ryu Yukawa, Shingo Yamamoto, Rei Hobara, Kazushi Fujikawa, Hiroshi Sakama, and Iwao Matsuda. Electron–hole recombination time at tio2 single-crystal surfaces: Influence of surface band bending. *The Journal of Physical Chemistry Letters*, 5:1953–1957, 6 2014.

[33] Janusz Bogdan, Joanna Pławińska-Czarnak, and Joanna Zarzyńska. Nanoparticles of titanium and zinc oxides as novel agents in tumor treatment: a review. *Nanoscale Research Letters*, 12:225, 12 2017.

[34] Yoshio Nosaka and Atsuko Y. Nosaka. Generation and detection of reactive oxygen species in photocatalysis. *Chemical reviews*, 117 17:11302–11336, 2017.

[35] Haijun Zhang, Yongfeng Shan, and Lijun Dong. A comparison of tiolt;subgt;2lt;/subgt; and zno nanoparticles as photosensitizers in photodynamic therapy for cancer. *Journal of Biomedical Nanotechnology*, 10:1450–1457, 8 2014.

[36] Joseph W. Nichols and You Han Bae. Odyssey of a cancer nanoparticle: From injection site to site of action. *Nano Today*, 7:606–618, 12 2012.

[37] Kyriakos Bourikas, Christos Kordulis, and Alexis Lycourghiotis. Titanium dioxide (anatase and rutile): Surface chemistry, liquid–solid interface chemistry, and scientific synthesis of supported catalysts. *Chemical Reviews*, 114:9754–9823, 10 2014.

[38] Gregor Žerjav, Krunoslav Žižek, Janez Zavašnik, and Albin Pintar. Brookite vs. rutile vs. anatase: What‘s behind their various photocatalytic activities? *Journal of Environmental Chemical Engineering*, 10:107722, 6 2022.

[39] Jingkun Jiang, Günter Oberdörster, Alison Elder, Robert Gelein, Pamela Mercer, and Pratim Biswas. Does nanoparticle activity depend upon size and crystal phase? *Nanotoxicology*, 2:33–42, 1 2008.

[40] Jan Wróbel and Jacek Piechota. Structural properties of zno polymorphs. *Physica Status Solidi*, 244:1538–1543, 5 2007.

[41] Francesca Scarpelli, Teresa F. Mastropietro, Teresa Poerio, and Nicolas Godbert. Mesoporous tio2 thin films: State of the art, 6 2018.

[42] Perkin Elmer. An introduction to fluorescence spectroscopy, 2000.

[43] ThermoFisher. Singlet oxygen sensor green product information, 2022.

[44] C. Burgess. Chapter 1 the basics of spectrophotometric measurement, 2007.

[45] Huanhuan Liu, Philippe J. H. Carter, Adrianus C. Laan, Rienk Eelkema, and Antonia G. Denkova. Singlet oxygen sensor green is not a suitable probe for 1o2 in the presence of ionizing radiation. *Scientific Reports*, 9:8393, 12 2019.

[46] Meng Li, Jun-Jie Yin, Wayne G. Wamer, and Y. Martin Lo. Mechanistic characterization of titanium dioxide nanoparticle-induced toxicity using electron spin resonance. *Journal of Food and Drug Analysis*, 22:76–85, 3 2014.

[47] Enze Li, Yi Sun, Guixiang Lv, Feng Qin, Xiyu Zhang, Zhiguo Zhang, Rui Zhang, Zheng Hu, and Wenwu Cao. The abnormal physicochemical phenomena of singlet oxygen sensor green in water in the presence of ultrasound. *ChemistrySelect*, 6:6631–6635, 7 2021.

[48] B.J. Parsons. Sterilisation of healthcare products by ionising radiation: principles and standards, 2012.

[49] Erzsébet Illés, Anna Tegze, Krisztina Kovács, Gyuri Sági, Zoltán Papp, Erzsébet Takács, and László Wojnárovits. Hydrogen peroxide formation during radiolysis of aerated aqueous solutions of organic molecules. *Radiation Physics and Chemistry*, 134:8–13, 5 2017.

[50] John P. Hunt and Henry Taube. *Journal of the American Chemical Society*, 74:5999–6002, 12 1952.

[51] Robert C. Mackenzie and Mowbray Ritchie. *Proceedings of the Royal society of London. Series A. Mathematical and Physical Sciences*, 185:207–224, 2 1946.

A | Appendix

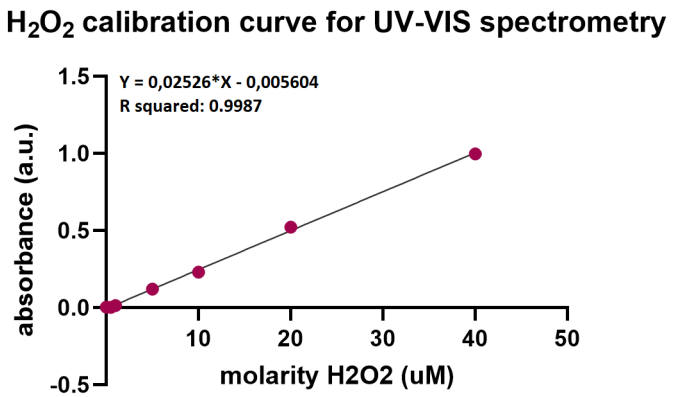

Figure A.1: The calibration curve used to convert absorbance (a.u.) to H_2O_2 molarity (μM) for UV-VIS experiments. The line formula and the corresponding R squared are given in the left corner of the graph. The samples were prepared as follows: 800 μL of TiO_2 solutions with known molarities + 100 μL potassium iodide stock solution + 100 μL ammonium molybdate stock solution

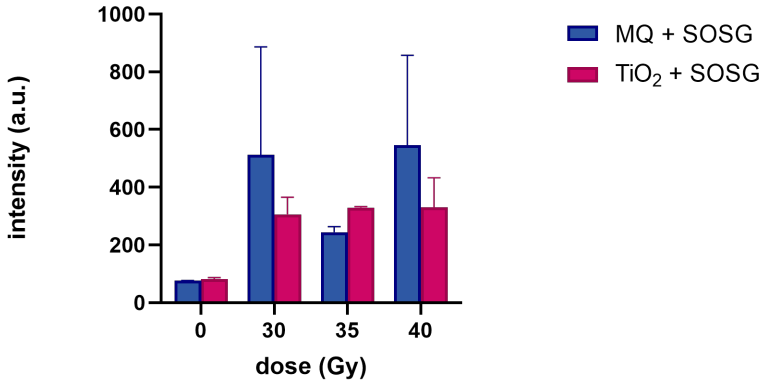

Figure A.2: Singlet oxygen detection: the maximum peak intensity (a.u.) measured by fluorescence spectroscopy for samples consisting of either 0.5 mL TiO_2 (0.5 g/L) solution or MilliQ water, added to 0.5 mL of SOSG probe solution (2 μL). The samples were irradiated with a Co-60 gamma source with doses 30 - 40 Gy. The error bars represent the standard deviation of the three samples analysed per dose. The samples for doses 30 and 40 Gy were the only samples that were ultrasonicated before irradiation.

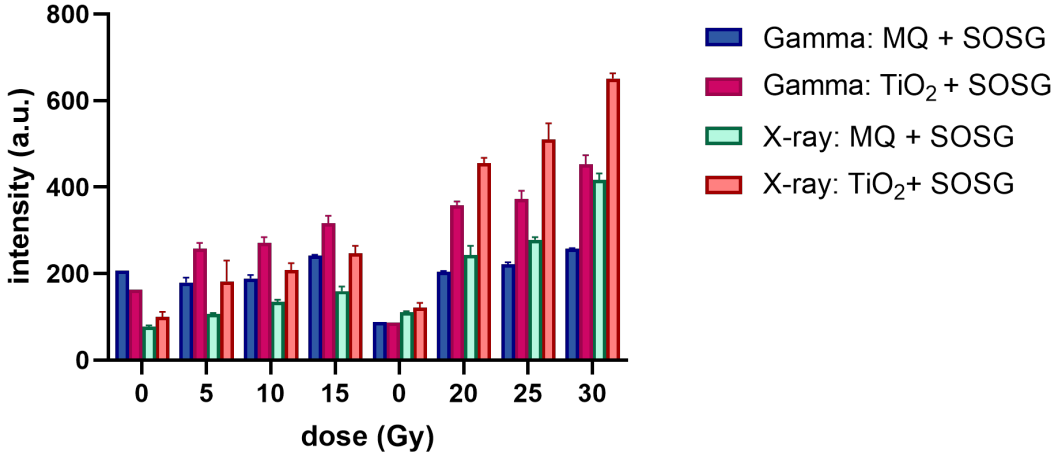

Figure A.3: Singlet oxygen detection: comparison between the data sets of X-ray and gamma irradiated samples (range 5 - 30 Gy) consisting of either 0.5 mL TiO_2 (0.5 g/L) solution or MilliQ water, added to 0.5 mL of SOSG probe solution (2 μL). The data from the different batches from subsection 4.1.1 and subsection 4.1.2 were not scaled as was done in Figure 4.3. The error bars represent the standard deviation of the intensities measured during fluorescence spectroscopy.

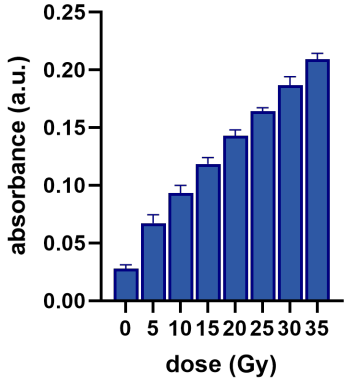

Figure A.4: Hydrogen peroxide detection: absorbance (a.u.) measured at 350.0 nm in UV-VIS spectroscopy for samples consisting out of 800 μL MilliQ water, with 100 μL potassium iodide and 100 μL ammonium molybdate stock solutions added between irradiation and the spectroscopic analysis. The samples were irradiated with a Co-60 gamma source with doses 5 - 35 Gy. The error bars represent the standard deviation of the 3 samples that were analysed per dose. The equivalent molarity graph is shown in Figure 4.4

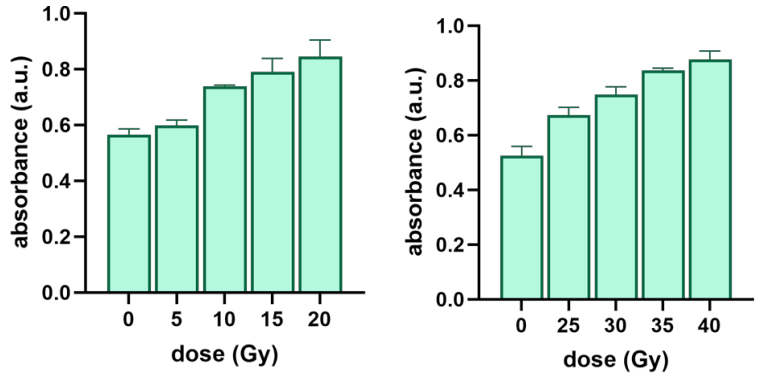

(a) 5 - 20 Gy **(b)** 25 - 30 Gy

Figure A.5: Hydrogen peroxide detection: absorbance (a.u.) measured at 350.0 nm in UV-VIS spectroscopy for samples consisting out of 800 μL ZnO solution (0.5 g/L), with 100 μL potassium iodide and 100 μL ammonium molybdate stock solutions added between irradiation and the spectroscopic analysis. The samples were irradiated with a Co-60 gamma source with doses 5 - 40 Gy in two batches. The error bars represent the standard deviation of the 3 samples that were analysed per dose. The equivalent molarity graphs are shown in Figure 4.5.

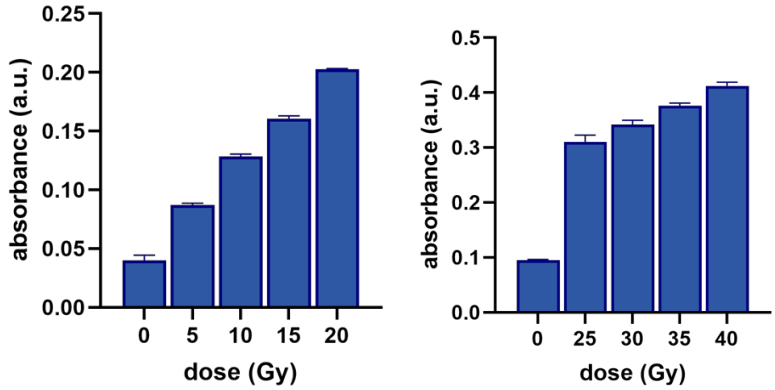

(a) 5 - 20 Gy **(b)** 25 - 40 Gy

Figure A.6: Hydrogen peroxide detection: absorbance (a.u.) measured at 350.0 nm in UV-VIS spectroscopy for samples consisting out of 800 μL MilliQ water, with 100 μL potassium iodide and 100 μL ammonium molybdate stock solutions added between irradiation and the spectroscopic analysis. The samples were irradiated with an X-ray source with doses 5 - 40 Gy in two batches. The error bars represent the standard deviation of the 3 samples that were analysed per dose. The equivalent molarity graph is shown in Figure 4.6.

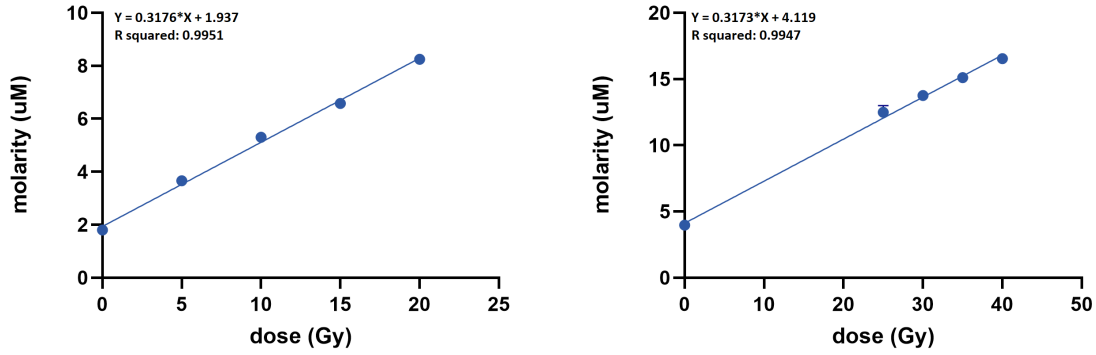

(a) 5 - 20 Gy **(b)** 25 - 40 Gy

Figure A.7: XY plots of Figure 4.6a and Figure 4.6b to show the linearity of the trend. The formulas and R^2 are given in the upper left corner of the plots. These graphs display the results of the hydrogen peroxide detection.

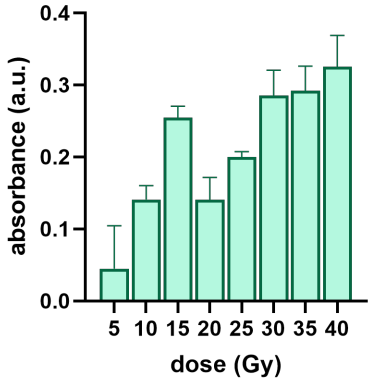

Figure A.8: Hydrogen peroxide detection: absorbance (a.u.) measured at 350.0 nm in UV-VIS spectroscopy for samples consisting out of 800 μL ZnO solution, with 100 μL potassium iodide and 100 μL ammonium molybdate stock solutions added between irradiation and the spectroscopic analysis. The samples were irradiated with an X-ray source with doses 5 - 40 Gy. The displayed values are the means of the absorbance values per dose that had the mean background absorbance (0 Gy) subtracted from them. The error bars represent the standard deviation and the equivalent molarity graph is shown in Figure 4.7.

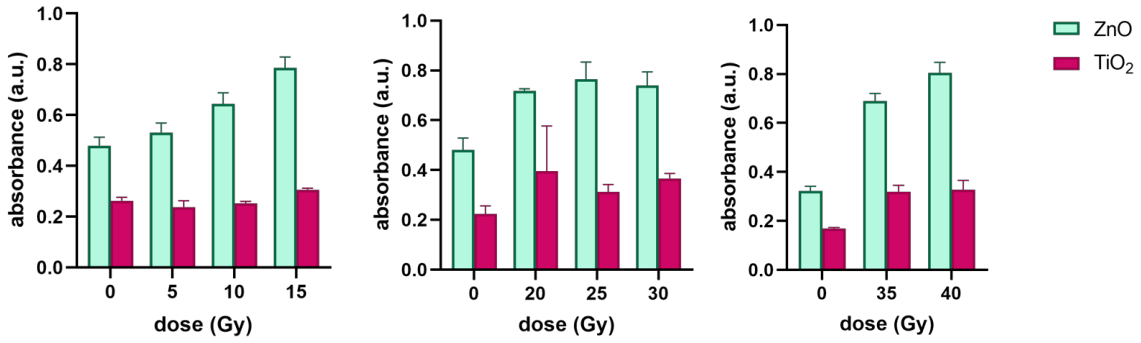

(a) 5 - 15 Gy **(b)** 20 - 30 Gy **(c)** 35 - 40 Gy

Figure A.9: Hydrogen peroxide detection: absorbance (a.u.) measured at 350.0 nm in UV-VIS spectroscopy for samples consisting of 800 μL of either a TiO_2 or a ZnO solution (0.5 g/L), with 100 μL potassium iodide and 100 μL ammonium molybdate stock solutions added between irradiation and the spectroscopic analysis. The samples were irradiated with a Co-60 gamma source with doses in the range of 5 - 40 Gy in three batches. The error bars represent the standard deviation of the 3 samples that were analysed per dose. The equivalent molarity graphs are shown in Figure 4.9.